Geochimica et Cosmochimica Acta 395 (2025) 248–266

Contents lists available at ScienceDirect

Geochimica et Cosmochimica Acta

journal homepage: www.elsevier.com/locate/gca

Metallogeny of subcontinental lithospheric mantle driven by sulfide-saturated pyroxenite-forming melts: evidence from the Balmuccia peridotite massif

Bartosz Pieterek[a,*], Magdalena Matusiak-Małek[b], Riccardo Tribuzio[c,d,e], Marina Lazarov[f], Magdalena Pańczyk[g], Harald Strauss[h], Thomas Kuhn[i], Zbigniew Czupyt[g], Jakub Ciazela[j], Stefan Weyer[f]

[a] *Geohazard Research Unit, Institute of Geology, Adam Mickiewicz University in Poznań, Poznań, Poland*
[b] *Institute of Geological Sciences, University of Wrocław, Wrocław, Poland*
[c] *Department of Earth and Environmental Sciences, University of Pavia, Pavia, Italy*
[d] *Institute of Geosciences and Earth Resources, C.N.R., Pavia Unit, Pavia, Italy*
[e] *National Institute of Oceanography and Applied Geophysics, Trieste, Italy*
[f] *Institute of Earth System Sciences, Section Mineralogy, Leibniz University Hannover, Hannover, Germany*
[g] *Polish Geological Institute - National Research Institute, Warsaw, Poland*
[h] *Institut für Geologie und Paläontologie, Universität Münster, Münster, Germany*
[i] *Federal Institute for Geosciences and Natural Resources (BGR), Hannover, Germany*
[j] *Institute of Geological Sciences, Polish Academy of Sciences, Wrocław, Poland*

ARTICLE INFO

Associate editor: Hassan Helmy

Keywords:
Melt-mantle reactions
Isotope fractionation
Chalcophile elements
Sulfide segregation
Metal budget

ABSTRACT

Focused melt flow is a common phenomenon in the subcontinental lithospheric mantle. Although it exerts significant control on the magmatic differentiation of the upper mantle, its role in metal transport remains poorly constrained. To improve our understanding of the subcontinental mantle metallogeny, we investigated the Balmuccia massif of the Ivrea-Verbano Zone (Italian Alps), which consists of fresh mantle peridotites that experienced a prolonged period of multistage melt intrusions. As a result, this massif hosts two suites of pyroxenite dykes, known as Cr-diopside and Al-augite pyroxenites, which enable us to provide undisturbed insights into mantle metallogeny. Here, through scrutiny of the pyroxenite dykes and their contacts with mantle peridotites, we provide insights into the sulfide and associated chalcophile metals (e.g., Cu and Ag) distributions. We demonstrate that the Balmuccia mantle pyroxenites are enriched in magmatic sulfides and sulfide-loving elements compared to the Balmuccia mantle peridotites. In particular, the pyroxenites contain up to 8 times more Cu (on average 227 ± 58 ppm; 1SD; n = 8) than the mantle peridotites (29 ± 20 ppm Cu; n = 20). Additionally, we found that each sulfide phase has distinct S-Fe isotopic signatures among sulfides. Such differentiation indicates that the S-Fe isotopic fractionation is most likely controlled by the mass-dependent fractionation that follows the (re)crystallization under high-T subsolidus magmatic conditions.

The increased amount of sulfides and associated chalcophile metals (Cu and Ag) within the studied pyroxenites evidence the heterogeneous distribution of sulfides and metals in the subcontinental lithospheric mantle, similarly to observations from other pyroxenite dykes within mantle rocks and metasomatized mantle xenoliths. Specifically, we estimate that from 12% to 42% of the Cu and from 11% to 40% of the Ag of the upper mantle inventory could be accumulated within mantle pyroxenites. Our results indicate that mantle pyroxenites constitute a critical metal reservoir for subcontinental lithospheric metallogeny.

---

* Corresponding author.
E-mail address: barpie@amu.edu.pl (B. Pieterek).

https://doi.org/10.1016/j.gca.2025.03.007
Received 26 October 2024; Accepted 8 March 2025

1. Introduction

Pyroxenites have been widely documented within mantle peridotites of subcontinental mantle origin, both in xenoliths and mantle exposures at the Earth's surface (Dantas et al., 2007; Downes, 2007; Python et al., 2008; van Acken et al., 2010; Xiong et al., 2014; Saunders et al., 2016; Borghini et al., 2016; Basch et al., 2019; Zou et al., 2019; Chen et al., 2020; Zhang et al., 2022), evidencing their common occurrence and important role in shaping the subcontinental lithosphere. The contribution of mafic–ultramafic dykes and layers to the lithospheric mantle is estimated to range from < 2 % according to calculations based on the depleted isotopic composition of mid-ocean ridge basalt (Petermann and Hirschmann, 2003) to up to 10 % based on field investigations (Pearson, 1996), with the most common contribution value of 5 % (Bodinier and Godard, 2003). The origin of pyroxenites hosted by mantle massifs or mantle pyroxenite xenoliths is still under discussion. They are mainly interpreted to be formed by melt-peridotite reaction (Bodinier et al., 2008) and/or mineral accumulation from the migrating basaltic melts (Rampone et al., 2020). Upper mantle pyroxenites can also be formed by residual and partially molten oceanic crust recycled during subduction (Montanini et al., 2012). Independently of genetic processes, pyroxenites are often enriched in sulfides compared to the host peridotites (Lorand, 1989a; van Acken et al., 2010; Wang and Becker, 2015b; Chen et al., 2020; Fang et al., 2024). Therefore, sulfide-bearing mantle pyroxenites are the prime targets for investigating the upper mantle evolution and for a better understanding of metal transfer and their potential genetic links with crustal sulfide mineralized domains.

Based on experimental studies, Wang et al. (2023) reported that the subcontinental lithospheric mantle affected by channelized melt flows and melt-peridotite reactions is favorable for driving upwards µm- to mm-scale sulfide droplets. The relatively dense sulfide liquid in the ascending silicate magmas is not prone to be transported upwards and tends to coalesce and settle. However, recent experimental and petrological observations evidence that hydrous minerals (Ezad et al., 2024a) or carbon, as a buoyant supercritical CO_2 fluid (Blanks et al., 2020; Cherdantseva et al., 2024a; Cherdantseva et al., 2024b; Ezad et al., 2024b) might be a covert agent promoting the physical transport of sulfides and metals upwards across the subcontinental lithospheric mantle. Therefore, the mobilization of deeply-rooted sulfides by these agents may facilitate the metal transport from the mantle to the lower-to-mid continental crust (Blanks et al., 2020) and may be possibly revealed by the presence of sulfide-rich mafic–ultramafic domains (Garuti et al., 2001; Locmelis et al., 2016; Holwell et al., 2022; Cherdantseva et al., 2025).

The melts migrating through the upper mantle interact with the peridotites triggering metasomatism and refertilization, particularly along wall rocks of melt conduits (Wang and Becker, 2015b; Belousov et al., 2021). Such melt migration results in compositional heterogeneity of the mantle and can be traced by the investigation of silicates (Montanini and Tribuzio, 2015; Borghini et al., 2020; Rampone et al., 2020). However, little attention was paid to the role and contribution of sulfides to this process. Additionally, the extent of sulfide-driven refertilization of wall rock peridotites is fundamentally unknown and should be addressed to constrain metal transfer better.

To elucidate the role of mantle pyroxenites in mantle metal refertilization, we selected the Balmuccia peridotite massif (Ivrea-Verbano Zone, NW Italy), one of the most comprehensively studied mantle bodies exposed at the Earth's surface (Shervais, 1979; Shervais and Mukasa, 1991; Mukasa and Shervais, 1999; Weyer et al., 2003; Mazzucchelli et al., 2009; Pistone et al., 2017; Beltrando, 2021; Decarlis et al., 2023). In contrast to metasomatized mantle rocks rich in hydrous phases, such as PIC (phlogopite, ilmenite and clinopyroxene) and MARID (mica, amphibole, rutile, ilmenite and diopside) suites, which may be an important reservoir for magmatic Ni-sulfide ore systems (Ezad et al., 2024a; Blanks et al., 2025), mantle pyroxenites hosted by the Balmuccia peridotite massif are exceptionally fresh, with lack of any evidence for forms of metasomatism (e.g., hydrous or carbonate) or crustal recycled materials (Zou et al., 2019). The fresh magmatic rocks enable us to carry out a comprehensive investigation of sulfide segregation within the pristine mantle body (Mukasa and Shervais, 1999; Mazzucchelli et al., 2009; Wang and Becker, 2015b). As these pyroxenites include higher amounts of magmatic sulfides and associated metals than adjacent peridotites (Garuti et al., 1984; Wang and Becker, 2015b; Wang et al., 2018b; Zou et al., 2019), their exposures constitute the best natural laboratory for providing new insights into the upper mantle metallogeny. Even though the Balmuccia pyroxenites were previously mainly studied utilizing whole-rock chemical and isotopic methodologies (Garuti et al., 1984; Wang et al., 2013; Wang and Becker, 2015a; Wang and Becker, 2015b; Wang et al., 2018b; Zou et al., 2019), their role in the metal flux and metallogeny of the subcontinental lithospheric mantle remains unidentified. We addressed this knowledge gap through the sulfide-based investigations of pyroxenite-peridotite transects and showed that mantle pyroxenites constitute a critical metal reservoir for subcontinental lithospheric metallogeny.

Current isotopic studies report variations of S and Fe isotopes indicating their fractionation among sulfide phases during magmatic cooling of the melt and sulfides (re)crystallization (LaFlamme et al., 2016; Brzozowski et al., 2021). However, none of these works reported the S-Fe isotopic signatures for the entire polyphasic magmatic sulfide assemblages, including all the present sulfide phases in the mantle rocks. For instance, the partitioning of Fe isotopes within the magmatic sulfide assemblages, including pentlandite, is poorly understood. In this study, we took advantage of the fact that the Balmuccia pyroxenites include large, polyphase sulfide grains (sometimes exceeding 1 mm in size) suitable for conducting *in situ* isotopic analyses, and we provided constraints about the fractionation of both traditional (S) and nontraditional (Fe) stable isotopes among sulfides during the (re)crystallization of sulfide melts. Such an approach provides previously inaccessible insights into the fractionation of isotopes between the sulfide phases that cannot be uncovered utilizing whole-rock investigations.

Altogether, through scrutiny of the distribution of sulfides and associated metals and determining the role of pyroxenite layers and dykes in sulfide segregation, we advanced our understanding of the metallogeny processes in the subcontinental lithospheric mantle. The adopted methodology also allowed us to assess how the mantle pyroxenites contribute to the metal budget of the subcontinental lithosphere.

2. Geological setting

2.1. Petrogenesis of studied samples

The Balmuccia peridotite massif is an NNE-trending, elongated km-sized fragment of the subcontinental lithospheric mantle located within the Ivrea-Verbano Zone (IVZ). It is located near the Insubric tectonic lineament, which separates the IVZ from the Austro-Alpine domain (Fig. 1a) (Sinigoi et al., 1983; Quick et al., 1995; Beltrando, 2021), and exposes fresh mantle rocks intruded by various generations of dykes. The Balmuccia peridotite massif retains magmatic contacts (known as Contact Series zone) with the surrounding lower crustal rocks of the Mafic Complex, a km-scale gabbroic intrusion formed during the post-collisional phase of the Variscan orogeny (Shervais and Mukasa, 1991; Mukasa and Shervais, 1999; Quick et al., 2003; Pieterek et al., 2024). The current position of the Balmuccia peridotite massif is a consequence of tectonic processes, such as rotation and uplift, during Mesozoic extension and Alpine compression (Handy et al., 1999; Mazzucchelli et al., 2009; Pistone et al., 2017; Decarlis et al., 2023).

The Balmuccia peridotite massif is predominantly composed of fresh lherzolites, associated with rare harzburgites and dunites, which are crosscut by various generations of mafic–ultramafic layers and dykes (Mukasa and Shervais, 1999; Wang and Becker, 2015b). These rocks constitute ~ 5 vol% of the massif (Decarlis et al., 2023). The Balmuccia peridotites were depleted by partial melting (~5–10 %; Weyer et al.,

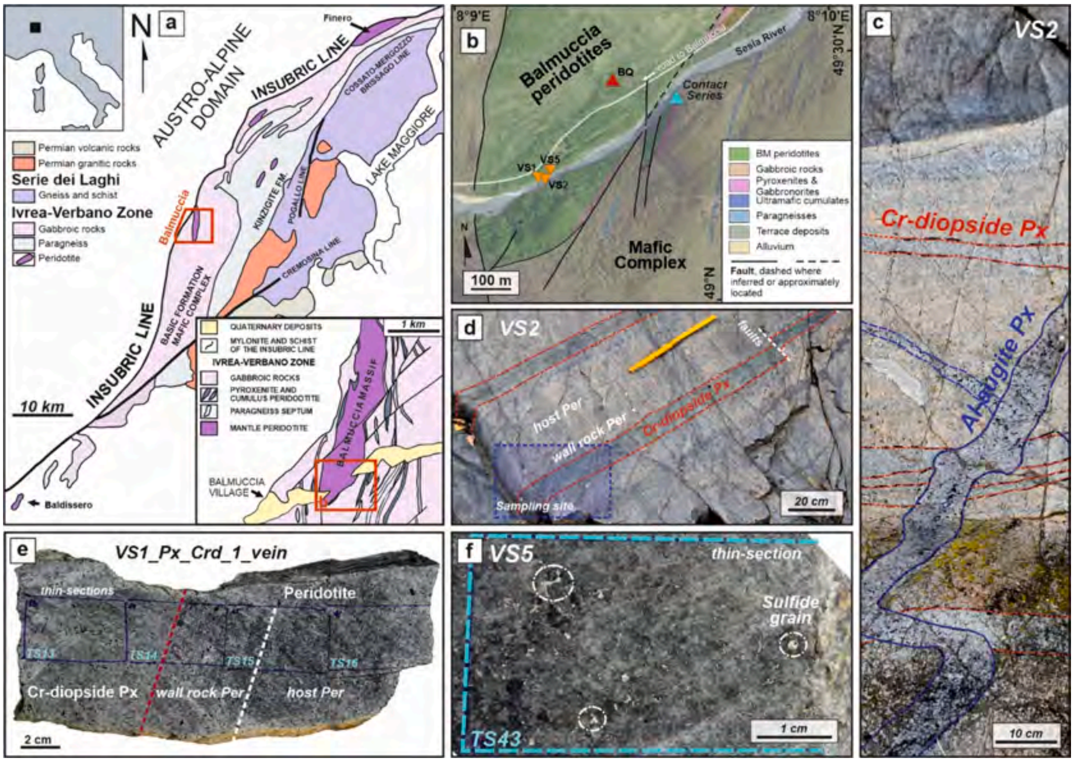

Fig. 1. Geological setting of the Ivrea-Verbano Zone (IVZ) and pyroxenite dykes within the Balmuccia mantle massif. (a) Simplified geological map of the IVZ, depicting its generalized stratigraphy and main mantle peridotite bodies localized mostly near the Insubric Line. The inset displays the close-up of the geological map of the Balmuccia mantle massif (BM) and the adjacent Mafic Complex (MC) (Sinigoi et al., 2010). (b) Geological map displaying the internal geological settings with sampling sites corresponding to the simplified lithological profile presented in Fig. 2. The background image has been produced using ©2023 Maxar satellite image. (c) Crosscutting relationships between two pyroxenite domains within the Balmuccia mantle massif. (d) Field image of the VS2 sampling site, displaying the sub-parallel layers of Cr-diopside pyroxenites characterized by sharp contacts with host peridotites. (e) An example of the investigated transect from the central part of the pyroxenite layer through the contact, wall rock peridotite (4-cm-thick layer), and host peridotite. TS means thin-section. (f) Zoom-in image of the thin-section billet portraying the distribution of sulfide grains within the central part of the Cr-diopside pyroxenite dyke (TS43). Only the largest sulfide grains have been marked by dashed circles. All bright spots indicate the location of sulfide grains.

2003; Decarlis et al., 2023) and melt extraction ca. 370 Ma (Ogunyele et al., 2024) and underwent nearly contemporaneous variable chemical re-equilibration processes within the mantle due to interaction with migrating melts leading to the formation of the pyroxenite dykes (Wang et al., 2013; Decarlis et al., 2023). Based on the mineralogy of pyroxenes and relative crosscutting relationships, the dykes were subdivided into two main groups: 1) an older Cr-diopside suite (websterites, olivine-websterites, and orthopyroxenites), mostly concordant with Balmuccia peridotite NE-SW-trending foliation (Wang et al., 2013), and 2) a younger, syn- to post-kinematic Al-augite suite (spinel clinopyroxenite and spinel-poor websterites) (Shervais, 1979; Sinigoi et al., 1983; Mukasa and Shervais, 1999; Mazzucchelli et al., 2009; Wang and Becker, 2015b). Additionally, during the crustal emplacement, the external parts of the massif, close to the Contact Series zone, were locally intruded by a late suite of gabbroic dykes with MORB-type geochemical signature (Voshage et al., 1988; Mayer et al., 2000; Rivalenti et al., 1995; Pieterek et al., 2024). Regarding these dykes represent distinct stages of origin from pyroxenite suites, they were not studied in this contribution.

In the field, the studied pyroxenites occur as layers and dykes typically displaying sub-vertical orientation and thickness ranging from a few mm to 1 m (Sinigoi et al., 1983; Obata and Karato, 1995; Mukasa and Shervais, 1999). Additionally, structural relationships evidence that studied pyroxenite suites were formed by several generations of melt injections. The Cr-diopside pyroxenite dykes represent the first stage of the mafic melt intrusion, possibly related to the refertilization of the depleted peridotites. These dykes are followed by a later Al-augite pyroxenite dyke generation. Overall, these dykes record a prolonged period of multistage melt intrusions into mantle peridotites before their crustal emplacement (Rivalenti et al., 1995; Mukasa and Shervais, 1999). The pyroxenites, in general, display sharp contacts with the enclosing peridotites (Mazzucchelli et al., 2009; Wang and Becker, 2015b). However, the contacting interface may reveal the occurrence of a reactive layer (Mazzucchelli et al., 2009). For instance, the Al-augite pyroxenite dykes are locally enveloped by a thin pyroxenite-reaction rim, whereas centimetre- to decimetre-wide dunitic bands in places occur at the contact between the Cr-diopside pyroxenite dykes and the host peridotites. In most cases, the Cr-diopside pyroxenites have a foliation that is concordant or sub-concordant to the foliation of enclosing peridotites, and the Al-augite suite displays isoclinal folds with axial planes (sub)parallel to the foliation (Sinigoi et al., 1983). Moreover, Beltrando (2021) provided evidence that the observed deformation pattern was produced entirely during the pure shear flow regime in which the regional foliation developed.

The two pyroxenite suites were interpreted as cumulates crystallized from S-saturated melts uprising from the asthenosphere during multistage late melt influx ca. 370 Ma (Ogunyele et al., 2024) into stretched continental lithospheric mantle (Wang and Becker, 2015b). The Nd-Sr isotope signature of both pyroxenite suites reveal restricted variations ranging between mid-ocean ridge basalt (MORB-) and ocean island basalt (OIB)-like values and are similar to those obtained for the enclosing peridotites (Sinigoi et al., 1983; Shervais and Mukasa, 1991; Rivalenti et al., 1995; Mukasa and Shervais, 1999). These constraints are consistent with the REE signature of clinopyroxenes investigated from the Cr-diopside suite showing the MORB-like affinity (Ogunyele et al., 2024). Notably, the highly siderophile and chalcophile element contents revealed strong fractionation of these elements between the studied pyroxenite suites during magma transport within the mantle (Wang and Becker, 2015b), caused by the magmatic evolution and interaction between the melts and enclosing peridotites.

2.2. *Sulfide and metal content characteristics*

In the Balmuccia peridotites, primary Ni-Cu-Fe polyphase sulfide grains are associated with spinel, typically in interstitial position to silicates, with a minor contribution of secondary sulfides (Garuti et al., 1984). The sulfide grains rarely exceed 500 μm in size; they are unevenly distributed throughout the rock, with an average frequency of 8–12 grains per cm^2. In places, small sulfide grains (10–30 μm) are enclosed in silicates (Wang et al., 2013; Wang et al., 2018b; Zou et al., 2019). Additionally, Garuti et al. (1984) reported extremely fine pyrite grains along alteration veins. The low proportion of sulfides in the peridotites is reflected in the average whole-rock Cu content from 26.1 ± 3.0 ppm ($n = 14$) (Garuti et al., 1984) to 29.2 ± 3.0 ppm Cu (Wang and Becker, 2015a; Huang et al., 2017).

In contrast to peridotites, the sulfides are relatively abundant in both Balmuccia-hosted pyroxenite suites. They typically form 50 − 500 μm polyphase grains, which locally exceed 1 mm in size. These grains mainly comprise pentlandite, chalcopyrite, and pyrrhotite (Wang et al., 2018b). Based on the mass balance calculations, it was documented that sulfide grains host > 98 wt% of the Cu budget of the pyroxenites (Zou et al., 2019). The whole-rock concentrations of S, chalcophile, and highly siderophile elements in the Balmuccia pyroxenites were subsequently investigated by Garuti et al. (1984) and Wang and Becker (2015a; 2015b). The early study of Garuti et al. (1984) reported that one pyroxenite dyke included high concentrations of Cu (97.5 ppm) and S (640 ppm). Consequently, the positive correlations observed between the S and sulfide-loving metals indicate that Balmuccia pyroxenites are sulfide- and metal-rich (see also Zou et al., 2019). Specifically, the S concentrations are up to one order of magnitude higher in pyroxenites (average value of 977 ppm, $n = 19$) than in peridotites (197 ppm ($n = 11$); Garuti et al. (1984) and 161 ppm ($n = 9$); Wang and Becker (2015a)). The same pattern is observed for Cu, with pyroxenite concentrations ranging from 90 to 484 ppm (average 189 ± 88 ppm (1SD), $n = 16$). In contrast to pyroxenites, the dunites hosted by Balmuccia peridotites have low S (<30 ppm) and Cu (<5 ppm) contents, except for one sample having 73 ppm of S and 25 ppm of Cu (Wang and Becker, 2015a). The whole-rock Cu isotopic signature of Balmuccia mantle rocks was also assessed (Huang et al., 2017; Zou et al., 2019), providing variable $\delta^{65}Cu$ values for peridotites (–0.13 ‰ to + 0.38 ‰) and pyroxenites (−0.66 ‰ to + 0.66 ‰).

3. Methods

3.1. *Sample collection and preparation*

To investigate the sulfide and associated metal distributions, we sampled 8 pyroxenite dykes comprising both Cr-diopside (6) and Al-augite (2) suites together with their adjacent peridotites (Fig. 1b), preparing 29 thin rock sections and 24 hand-sized samples for whole-rock analyses (Table S1). Additionally, four reference peridotites from the Balmuccia quarry, devoid of pyroxenites, were sampled and investigated by whole-rock and *in-situ* methods to complete the entire set of samples and provide a geochemical background. To prepare the pyroxenite-peridotite transects, we cut off the slices of the entire rock samples from which the thin section billets were cut out to prepare 50-μm-thick polished thin sections. For each pyroxenite-peridotite contact, we prepared thin section including both lithologies and defined them as ∼ 2-cm-thick wall rocks. The remaining fragments of the rocks were cut into pieces comprising the pyroxenite dyke, wall rock peridotite (4-cm thick) and host peridotite (Fig. 1d-e). Rock subsamples defined for whole-rock analyses were carefully cleaned with a Hermes SiC sandpaper (grit size P120) to remove potential saw contamination and washed in distilled water using an ultrasonic cleaner (3 times for 10 min). The rock slices were subsequently crushed to gravel fraction using a Retsch BB51 tungsten carbide jaw crusher. A representative portion (100–250 g) of the crushed material was ground by a tungsten swing mill at the Institute of Geological Sciences, University of Wroclaw, Poland.

3.2. *Petrographic description and quantitative mineralogy*

The general mineral composition of silicates (Table S1) and sulfide grains (Table S2) and their abundances in polished thin sections were determined under reflected light using Zeiss Axioplan 2 imaging optical microscope at the Institute of Geology, Adam Mickiewicz University in Poznań, Poland. Simultaneously with the petrographic description for most of the described sulfides, the reflected light images were taken and used for further analyses and calculations. Each sulfide grain was described, including the grain position with respect to silicates, the shape, and the approximate size (Table S2). This description allowed us to calculate the cumulative areas of polyphase sulfide grains and the areas of the different sulfide phases. In addition, detailed calculations of silicate modes were performed based on the point-counting method, utilizing the entire thin section images taken under transmitted light (plane and cross-polarized light) at the Institute of Geological Sciences, University of Wrocław, Poland, and analyzed using ImageJ (Roduit, 2007) software.

3.3. *Whole-rock analyses*

3.3.1. *Major and trace element compositions*

The major element data (Table S3) for the studied samples were determined using X-ray Fluorescence (XRF) spectroscopy at the Federal Institute for Geosciences and Natural Resources (BGR), Hannover, Germany. To measure the major element contents, pressed powder pellets were prepared and comprised 1 g of sample and 5 g of $LiBO_2$, which were mixed and melted for 20 min at 1200 °C. The tablets were analyzed with a wavelength-dispersive PANalytical AXIOS X-ray spectrometer equipped with a Rh X-ray tube. The X-ray spectrometer was calibrated using a total of ∼ 150 certified international reference materials. Total loss-on-ignition (LOI) was measured on pre-dried powders and after ignition at 1030 °C in a muffle furnace for 10 min. Specifically, the accuracies are mostly < 3 rel.% (RSD, relative standard deviation; relative values refer to the measurements in relation to used reference materials, expressing how close the measured value is to the reference value), with two exceptional values of 5.3 and 5.6 rel.% for Na_2O and MnO. Precisions are < 2 rel.% (RSD), with more varied values for Na_2O (9.1), K_2O (17.4), TiO_2 (9.1), and P_2O_5 (39.8 rel.%).

Trace element data (Table S3) were obtained at Activation Laboratories Ltd., Canada, utilizing the Ultratrace 5 analytical package, which is a combination of Instrumental Neutron Activation Analysis (INAA) and 4-acid digestion in a sequence of perchloric, hydrofluoric, hydrochloric, and nitric acids further, followed by analysis by Inductively Coupled Plasma Mass Spectrometry (ICP-MS). For all samples (except for WR75) > 30 g of powder was encapsulated in a polyethylene vial for INAA measurements to counteract the heterogeneous distribution of precious metals. A detailed description of the multi-method analysis is available in the Ultratrace 5 − Total Digestion − ICPMS, INAA subsection of the Methods section of the Actlab website (https://www.actlabs.com). Selected samples for the present study and Contact Series samples were measured within the same analytical session, and therefore, the accuracies and precisions are available in Pieterek et al. (2024), invariably < 20 rel.%. (RSD) The correlation matrix for major and trace elements is reported in Table S4.

3.3.2. *S isotopes*

The whole-rock S concentrations (Tables S3 and S5) were measured using an ELTRA CS580 carbon–sulfur analyzer at the Institut of Geology and Paleontology, University of Münster, Germany. Approximately 75–100 mg of sample powder and 0.4–0.9 g of V_2O_5 were placed in a porcelain crucible, combusted in an oxygen atmosphere at 1350 °C, and analyzed via infrared spectroscopy. The crucibles were beforehand heated to 1200 °C in a muffle furnace for several hours to remove potential sulfur compounds. We achieved a precision of 3.3 % (double relative standard deviation; 2RSD) and an accuracy of 3.6 % (2RSD) based on the reference material with 1.41 % S. Especially in those samples with low S content, the analyses have been duplicated (n = 5) to control the heterogeneity of the sample and S concentrations. We achieved a precision of 7.0 % (2RSD). Isotopic analyses were conducted at the same laboratory applying a sequential wet chemical technique following Canfield et al. (1986), thereby liberating acid volatile sulfide sulfur (AVS) and Cr-reducible sulfur (CRS). For all investigated dykes, the S was extracted sequentially as AVS and CRS, whereas for peridotites, except for sample WR16, the S was extracted together as Ag_2S (Table S5). In this study, the methodology was identical as described in Pieterek et al. (2024), using the same reference material (Vienna Canyon Diablo Troilite) and spectrometer. The average relative uncertainty of ± 0.06 ‰ (2σ) for $\delta^{34}S$ was achieved.

3.4. *In-situ analyses*

3.4.1. *Scanning electron microscope*

To characterize the microtextural relations occurring at the interface between pyroxenite dykes and hosting peridotites, we used a scanning electron microscope JEOL JSM-IT100 In-Touch-Scope™ with EDX Oxford detector at the Institute of Geological Sciences, University of Wrocław, Poland. Element distribution maps (Figs. S1-S4) of single frames were collected at a magnification of 50 times for whole sections, automatically merged, and divided into phases. Identification of each phase was conducted manually.

3.4.2. *Electron microprobe*

Major element composition of sulfides (Table S6) were determined using a Cameca SX-Five electron microprobe (EMPA) at the Laboratory of Electron Microscopy and Electron Probe Micro-Analysis of the Faculty of Geology, University of Warsaw, Poland. Standard materials for sulfides include oxides (CoO, NiO, and Fe_2O_3), sphalerite (S), chalcopyrite (Cu), and tellurites (Ag). The analyses were carried out with an acceleration voltage of 25 kV, a current of 15nA, and a focused beam. The detection limits, accuracy, and precision of the EPMA measurements are provided in Table S6.

3.4.3. *S isotope analyses*

To acquire in-depth insights into S isotope compositions, the whole-rock S isotope analyses were supplemented by *in-situ* ^{32}S and ^{34}S isotope measurements (Table S7) in sulfide phases (pyrrhotite, chalcopyrite, pentlandite, and pyrite). Analyses were conducted by Sensitive High-Resolution Ion Microprobe (SHRIMP Ile/MC) at the Micro-area Analysis Laboratory, Polish Geological Institute − National Research Institute (PGI-NRI), Warsaw, Poland. Rock subsamples (n = 12 for the entire profile) containing the largest sulfide grains were cut out from thin-section billets and sample remainders and mounted along with reference materials, including the Cpy1 and Cpy2 chalcopyrites (Li et al., 2020), Sudbury pyrrhotite (Fiege et al., 2014), JC-Po pyrrhotite and IC-Pn pentlandite (Chen et al., 2021), as well as Ruttan and Park City pyrites. The prepared mounts were embedded in epoxy resin, polished, and coated with gold. The analytical spots were selected using an optical microscope and BSE images using an SU3500 SEM (Hitachi, Tokyo, Japan) at the PGI-NRI. Analyzed sulfides were bombarded with a high energy primary beam of Cs + ions in a high vacuum with a spot diameter of 26 μm and a depth of < 5 μm. A different primary beam was used for the different sulfide phases, namely 5nA for pyrrhotite, 4nA for chalcopyrite, and 3nA for pentlandite and pyrite. The acceleration voltage of 15 kV and mass resolution (M/ΔM) of 2000 were used for all analyses. Data were reduced using the POXY software and are presented in Table S7.

Reference materials were measured at every three analytical spots to monitor the quality of the conducted analyses. The Sudbury pyrrhotite is characterized by a $\delta^{34}S$ reference value of + 2.4 ± 0.2 ‰ (1σ) measured in solution using the Kiba extraction method (Ripley et al., 2011). The obtained average value of + 2.41 ± 0.14 (2SD; n = 23) with an accuracy of 0.4 % (2RSD) and precision of 5.9 % (2RSD) matches the reference value. The S isotopic composition of the chalcopyrite reference materials was previously measured using secondary ion mass spectrometry by two independent laboratories (Centre for Ore Deposit and Earth Sciences at the University of Tasmania and Geochronology Laboratories, Chelmsford, MA); the $\delta^{34}S$ reference values are + 1.4 ± 0.2 ‰ (1σ) for the Cpy1 standard and − 0.7 ± 0.5 ‰ (1 σ) for the Cpy2 standard, respectively. During the analytical session, we obtained a reference value of + 1.41 ± 0.10 ‰ (2SD; n = 19) for Cpy1, revealing an accuracy of 0.8 % (2RSD) and a precision of 6.9 % (2RSD). The JC-Pn reference material has a $\delta^{34}S$ value of − 0.09 ± 0.15 ‰ (2SD) (Chen et al., 2021), whereas we obtained an average value of − 0.09 ± 0.23 ‰ (2SD; n = 38) with an accuracy of 0.6 % (2RSD). Although we measured two pyrite reference materials during an analytical session, our results were standardized to Rutan pyrite, which provided more consistent results than the Park City pyrite, yielding an average $\delta^{34}S$ value of 1.20 ± 0.29 ‰ (2SD; n = 10).

3.4.4. *Fe isotope analyses*

The Fe isotopes of sulfides (pyrrhotite, chalcopyrite, and pentlandite) were measured using a femtosecond laser ablation system (fs-LA) (based on a Spectra-Physics Solstice, USA) coupled to a NeptunePlus (Thermo Scientific, Germany) multi-collector (MC) ICP-MS at the Institute of Earth System Sciences, Leibniz University Hannover, Germany. Measurements were carried out as described by Horn et al. (2006) and Oeser et al. (2014) and results were reported relative to IRMM-014 standard as $\delta^{56}Fe$ and $\delta^{57}Fe$ (i.e., deviations of $^{56}Fe/^{54}Fe$ and $^{57}Fe/^{54}Fe$ relative to the IRMM-014 standard expressed in ‰). Notably, we used a Ni standard solution (NIST SRM 986) for mass bias correction of pyrrhotite and chalcopyrite, however, only sample-standard bracketing without Ni mass bias monitor for pentlandite (as the latter contains a significant amount of Ni). In addition, an in-house JM puratronic (PURA) Fe-standard (99.995 % Puratronic, Johnson Matthey, lot No. FE495007IF2) was measured at the beginning of and within each analytical session to verify that both, $\delta^{56}Fe$ values with and without Ni mass bias correction agree with those previously reported by Horn et al. (2006) and Oeser et al. (2014). For each analytical session, the average $\delta^{56}Fe$ values of PURA, including Ni mass bias correction, is reported in Table S8. All sulfides and standards were ablated along 45- to 60-μm-wide lines that, in most cases, created raster to provide a stable analytical signal. The laser frequencies of 11–20 Hz for standards and 25–125 Hz for sulfides were used. We have achieved a double standard deviation of replicate standard measurements (2 RSE) of < 0.1 ‰ (in $\delta^{56}Fe$; Table S8).

4. Results

4.1. *Characteristics of peridotite-pyroxenite textural relationships*

The investigated Balmuccia-hosted layers and dykes are classified as websterites and comprise anhedral grains of clinopyroxene and orthopyroxene and minor amounts of olivine, sulfides, and spinel (Fig. S1a). Pyroxenes form anhedral, slightly elongated crystals contacting at triple-points, whereas olivine occurs as inclusion within orthopyroxene. The host and wall rock peridotites are formed of olivine, orthopyroxene, clinopyroxene, and spinel, characterized by protogranular texture (Table S1). Utilizing the EDS-based thin section maps, we reported different textural characteristics of the peridotite-pyroxenite contacts (Figs. 2a-c and S1-S4). Considering the contacts between the thick (>4 cm up to 20 cm) Cr-diopside websterite dykes and wall rock peridotite,

Table 1
Compilation of the sulfides' characteristics together with the whole rock Cu, Ag, and S contents and S isotope signatures for the studied Balmuccia mantle pyroxenites and hosting peridotites. The original data are reported in the Supplementary Tables.

		Reference Per	Host Per	Wall rock Per	Wall rock Cr-diopside Px	Cr-diopside Px	Wall rock Al-augite Px	Al-augite Px
Number of thin sections	Thin section measurements	4	8	15	4	7	2	2
Average sulfide content [vol‰]		0.28 ± 0.28	0.21 ± 0.10	0.28 ± 0.34	2.97 ± 2.24	3.11 ± 4.22	0.85 ± 0.67	1.04 ± 0.57
Range of sulfide content [vol‰]		0.10 – 0.76	0.09 – 0.33	0.0004 – 1.22	1.17 – 6.79	0.96 – 13.42	0.18 – 1.51	0.47 – 1.60
Average pyrrhotite mode [%]		25.3 ± 13.7	15.8 ± 6.4	16.7 ± 11.4	14.1 ± 4.3	25.8 ± 6.3	23.1 ± 14.5	40.2 ± 26.8
Range of pyrrhotite mode [%]		6.0 – 41.1	8.3 – 26.4	0.9 – 36.1	6.8 – 17.2	14.3 – 33.3	8.7 – 37.6	13.4 – 67.0
Pyrrhotite average size [μm]		32.8 ± 17.7	29.4 ± 11.6	24.0 ± 14.2	51.7 ± 19.2	60.9 ± 35.9	43.4 ± 29.7	60.0 ± 35.9
Average chalcopyrite mode [%]		12.2 ± 7.0	6.5 ± 7.4	13.3 ± 13.2	13.4 ± 4.0	12.0 ± 4.1	21.6 ± 2.0	9.9 ± 1.9
Range of chalcopyrite mode [%]		3.4 – 22.6	0.0 – 21.3	0.0 – 49.6	9.5 – 20.0	4.6 – 17.4	19.6 – 23.6	8.0 – 11.7
Chalcopyrite average size [μm]		33.7 ± 12.6	27.6 ± 20.8	28.5 ± 19.2	55.7 ± 19.5	51.8 ± 21.3	56.5 ± 6.8	36.1 ± 2.9
Average pentlandite mode [%]		62.6 ± 20.4	77.6 ± 8.8	70.2 ± 16.0	72.4 ± 7.3	62.1 ± 7.6	55.3 ± 12.5	50.0 ± 25.0
Range of pentlandite mode [%]		36.3 – 90.6	63.0 – 91.4	35.0 – 95.4	63.2 – 83.7	50.1 – 76.2	42.8 –67.7	25.0 – 75.0
Pentlandite average size [μm]		53.2 ± 23.4	61.5 ± 13.0	54.1 ± 26.9	104.6 ± 26.9	100.2 ± 39.2	68.8 ± 21.8	62.3 ± 4.2
Number of samples	Whole rock analyses	4	8	8	n/a	6	n/a	2
Average Cu content [ppm]		31.1 ± 7.0	25.6 ± 14.0	30.3 ± 27.6		233.7 ± 65.4		206.0 ± 3.0
Average Ag content [ppb]		5.8 ± 1.5	6.6 ± 2.3	8.7 ± 6.3		64.2 ± 31.2		55.0 ± 2.0
Average S content [ppm]		154.5 ± 7.0	146.1 ± 65.5	150.4 ± 110.5		939.0 ± 408.5		851.1 ± 289.5
Average $\delta^{34}S$ [‰]		0.32 ± 0.22	0.23 ± 0.25	0.21 ± 0.33		0.44 ± 0.22		0.72 ± 0.25
Range of $\delta^{34}S$ [‰]		0.14 – 0.69	−0.27 – 0.51	−0.27 – 0.81		0.19 – 0.87		0.47 – 0.97

Per – peridotite; Px – pyroxenite. ± symbol refers to 1SD. The increased number of thin sections for wall rock peridotite is caused by the investigation of thin sections comprising contacts between peridotite and pyroxenite (see Table S2).

they are either sharp or transient and formed by clinopyroxene-rich zones parallel to the elongation of the vein. When the contact is sharp, the wall rock peridotite has a composition of lherzolite, when it is complex, the composition of peridotite is harzburgitic. In both types of contact, sulfides are concentrated, within the veins (also in the marginal clinopyroxene-rich layers), but a minor amount is observed also in the wall rock peridotite (Fig. S1b).

The texture of the Cr-diopside websterite dykes of moderate thickness (~3–4 cm) has sharp, but uneven contact with the wall rock peridotite (Fig. S2a). We observed 2–3 mm long anhedral crystals of clinopyroxene that penetrated the wall rock peridotite. A thin layer of orthopyroxene often underlines their contact with olivine. The same observation was provided for single crystals of olivine in the marginal parts of websterite dykes. In this case, the contact between olivine and clinopyroxene is also underlined by orthopyroxenes. In the amphibole-bearing dyke (e.g., TS48 and TS49), the occurrence of amphibole is strictly limited to the dyke and is evenly distributed within it. In most cases, amphibole forms anhedral grains at contact between phases (orthopyroxene and clinopyroxene or olivine and clinopyroxene). Sulfides are also associated exclusively to dyke and the clinopyroxene grains, which are not in direct contact with the dyke. Moreover, we observed that sulfides are not evenly distributed within the studied dykes. For example, some sectors of the dyke are sulfide-poor compared to the remaining part of the dyke (Fig. S2b). The wall rock peridotites of the considered dykes have harzburgitic composition.

The thin (≤1 cm) Cr-diopside websterite dykes are formed mostly of clinopyroxene, with minor amounts of orthopyroxene and olivine. The dykes are characterized by discontinuous rims of coarse-grained orthopyroxene (~5 mm in diameter). Olivine locally occurs as separate grains. The contact between the dyke and the wall rock peridotite is sharp but uneven (Fig. S3a). Sulfides occur primarily in the dyke, whereas only scarce grains were noticed in the peridotite (Fig. S3b). In the dykes where the clinopyroxene-rich core is thick, sulfides may be distributed unevenly (i.e., concentrate along one margin of the vein). Sulfide grains typically occur at contacts between clinopyroxene and orthopyroxene crystals. The wall rock peridotites have lherzolite compositions.

The Al-augite olivine websterite dykes consist of clinopyroxene, orthopyroxene, spinel, and minor sulfides. Pyroxenes form anhedral, slightly elongated crystals contacting at triple-points. The elongated grains are subparallel and define a weak linear texture. The anhedral, holy-leaf-shaped crystals of green spinel do not follow the lineation but are usually associated with amphibole and orthopyroxene. Contact of the Al-augite websterite dyke with the wall rock peridotite is sharp and underlined by the presence of clinopyroxene- and olivine-poor zone with coarse crystals of orthopyroxene (Fig. S4a). The wall rock peridotite has a composition of lherzolite. Sulfide grains in the dyke are associated with spinel and/or orthopyroxene but are unevenly distributed within the rock (Fig. S4b). Peridotites at the contact with the Al-augite dyke contain low amounts of sulfides but, where present, are also associated with orthopyroxene.

4.2. *Sulfide content and mineralogy*

In the 33 thin rock sections studied, we identified > 1900 individual, either monophasic or polyphasic, sulfide grains that are heterogeneously distributed throughout the dyke-scale transects. In particular, the highest sulfide amounts were observed for the pyroxenite dykes (816 grains in 9 thin sections; Table S2), with no systematic difference in the sulfide amount between the Cr-diopside and Al-augite pyroxenites. The central part of the pyroxenite dykes contain sulfides whose amount range between 0.43 and 13.42 vol‰ with an average of 2.65 ± 3.82 vol‰ (1SD; n = 9), with slightly lower values for the wall rock 2-cm thick contact (wall rock pyroxenite) with peridotites ranging from 0.18 to 6.79 vol‰ (average of 2.26 ± 2.13 vol‰; 1SD; n = 6) (Table 1). We found an almost 10 times decrease in sulfide content in the wall rock peridotites with respect to pyroxenites, which overall display an average content ranging from 0.0004 to 1.22 vol‰ with an average value of 0.3 ± 0.3 vol‰ (1SD; n = 15). Specifically, in the wall rock peridotites adjacent to thin pyroxenite dykes (samples TS45–46 and TS48–49), the sulfide content is 2–3 times lower than in the adjacent pyroxenites (Fig. 4). Compared to pyroxenites, the host peridotites are characterized by lower sulfide contents yielding a range from 0.09 to 0.33 with an average of 0.21 ± 0.10 vol‰ (1SD; n = 8). The reference value for country Balmuccia peridotites in this study is 0.12 ± 0.03 vol‰ (1SD; n = 3). However, one sample of reference peridotite collected from the Balmuccia quarry reveals an exceptionally high value of 0.71 vol‰ (Table S2) with respect to others from the same site. The same decreasing trend is observed for the average size of sulfides (Table 1). All sulfide phases (pyrrhotite – Pyh, [$Fe_{1-x}S$]; chalcopyrite – Ccp, [$CuFeS_2$]; pentlandite – Pn, [$(Ni,Fe)_9S_8$]) are significant within the central part of dykes and adjacent wall rock pyroxenites, displaying an average size of 61 and 49 µm for Pyh, 48 and 56 µm for Ccp, and 92 and 93 µm for Pn, respectively. The Balmuccia peridotites host sulfides with an average size of 27 µm for Pyh, 29 µm for Ccp, and 56 µm for Pn (Table S2).

The sulfides mainly occur as polyphase grains, except rare monophase pentlandite or chalcopyrite grains, forming mainly irregular and angular grains in the interstitial positions (>95 %) to silicates. The difference between the pyroxenite dykes and mantle peridotites is also highlighted by the morphology of the sulfides. On average, 72 % of sulfide grains hosted by the dykes and 71 % of the wall rock pyroxenites have an angular morphology, with decreasing contribution in peridotites: from 61 % for wall rock, 56 % for host, and 49 % for reference peridotites, respectively. Consequently, the contribution of rounded and elongated sulfide grains increases in the opposite trend from peridotites (28 and 16 %, respectively) to dykes (19 and 9 %, respectively) (Table S2). The sulfides form massive crystals typical for igneous origin with slight alteration by secondary sulfides, e.g., pyrite and bornite were recognized only in one sample of Al-augite pyroxenite (TS26 and 24) and Cr-diopside pyroxenite (TS04), respectively. In addition, cubanite ($CuFe_2S_3$) crystals occurring at the rims of sulfide grains in association with chalcopyrite were detected in nine thin sections, mainly within the pyroxenite dykes (Table S6). Furthermore, the dominant sulfides are locally associated with small (<20 µm) sulfide blebs or veinlets occurring along the crystal contacts and fractures that have not been accounted for in thin section-based calculations.

Based on sulfide mode calculations, we found that the Balmuccia peridotite-hosted sulfides are dominated by pentlandite (on average 71.0 %; n = 27). The contribution of pyrrhotite and chalcopyrite gradually increases, associated with a decrease of the pentlandite proportion, towards the pyroxenite dykes. Specifically, the inherent sulfides display different mean assemblages: 1) $Pyh_{16}Ccp_7Pn_{77}$for host peridotites, 2) $Pyh_{17}Ccp_{13}Pn_{70}$ for wall rock peridotites 3) $Pyh_{17}Ccp_{16}Pn_{67}$ for wall rock pyroxenites, and 4) $Pyh_{29}Ccp_{12}Pn_{59}$ for pyroxenites.

4.3. Whole-rock compositions

The degree of chemical evolution of the pyroxenite dykes is expressed by the whole-rock Mg-number (Mg# defined as 100 × [molar Mg/(molar Mg + molar Fe)]). In contrast to the nearly homogenous compositions of peridotites (e.g., average Mg# of 90.0 ± 0.7; 1SD; n = 22), the pyroxenite dykes display variable Mg# depending on the lithology. In the set of peridotites, we found two harzburgite samples with a high Mg# of 91.7–91.8. The Al-augite pyroxenites have lower Mg#

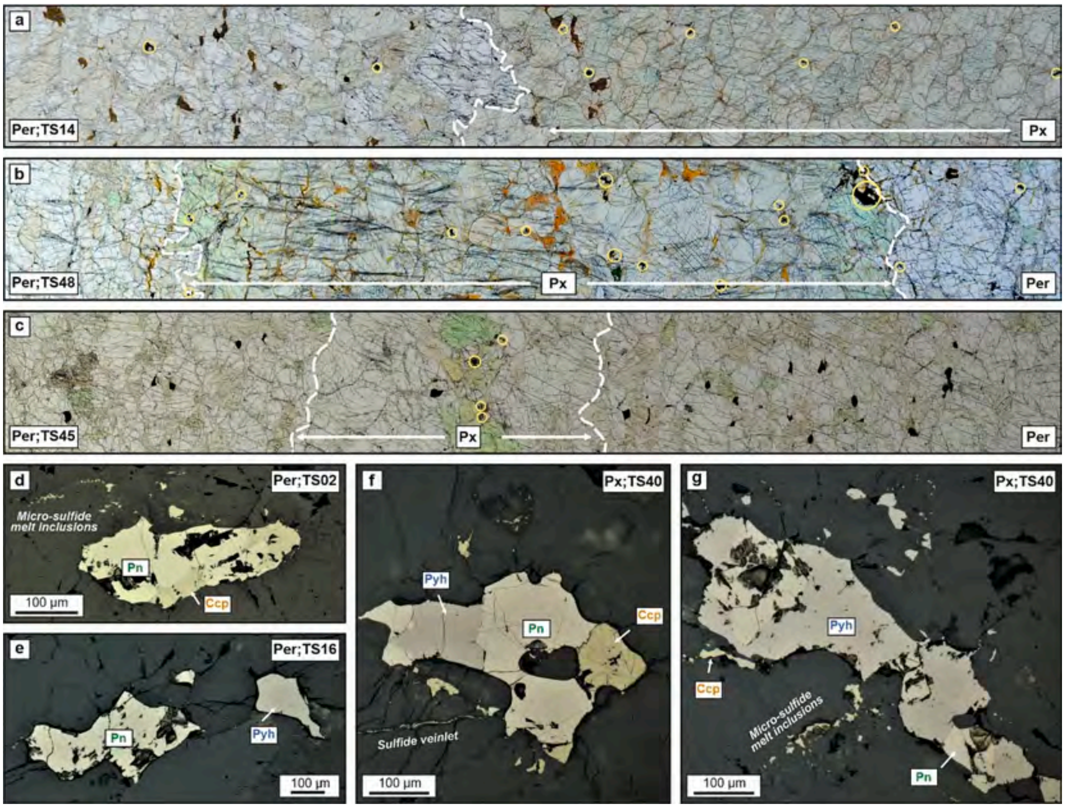

Fig. 2. Peridotite-pyroxenite (Per-Px) contact interfaces and sulfide textures observed in this study. (a-c) Examples of the studied contacts between the Balmuccia mantle peridotites and pyroxenites, highlighting the reactive contact interface of thick Cr-diopside websterite dyke (a), sharp contact interface of moderate thickness dyke (b), and thin (~<1 cm) Cr-diopside websterite dyke enveloped by orthopyroxene rims (c). All panels (a-c) are scaled the same having a 4-cm length. White arrows mark the extent of the pyroxenites whereas the white dashed lines defines the approximate margins of the studied dyke. Yellow circles mark the location of sulfides. (d-g) Polyphasic sulfide grains of the Balmuccia peridotites (d-e) and pyroxenite dyke (f-g) comprising pentlandite (Pn), chalcopyrite (Ccp), and pyrrhotite (Pyh) hosted interstitially to silicates. TS refers to the thin-section number.

(83.8–88.1) than the Cr-diopside pyroxenites (88.7–91.9, with an average of 90.1 ± 1.1, 1SD; n = 6) (Fig. 2). Independently of Mg# (Fig. 3a and Table S4), the increased content of sulfides in the pyroxenite dykes and their decreasing contribution in peridotites is expressed by the whole-rock metal contents. The sulfide-poor peridotites have on average 150 ± 81 ppm S (1SD; n = 20; ranging from 12 to 402 ppm S) and 29 ± 20 ppm Cu (1SD; n = 20; ranging from 2 to 97 ppm Cu), whereas the pyroxenite dykes display an average ~ 7-time increase of S content, which ranges from 491 to 1776 with an average value of 917 ± 384 ppm (1SD; n = 8), and ~ 8-time increase of Cu concentration, being between 170 and 367 ppm with an average of 227 ± 58 ppm (1SD; n = 8). The same trend is also expressed by Ag, which is low in peridotites (from below detection limits to up to 22 ppb; an average of 7 ± 4 ppb; 1SD; n = 20), and relatively high in pyroxenites (27–126 ppb, with an average of 62 ± 27 ppb, 1SD; n = 8). These elements overall provide the same trends, as expressed by high correlation values of $R^2 = 0.98$ for Cu vs. Ag and 0.96 for Cu vs. S (Fig. 3c-d). The correlation matrix calculations also document that Sc positively correlate with S in the pyroxenites ($R^2 = 0.91$). Additionally, the concentrations of Sr, Ga, Cs, Ce Zr, and Y are higher in the pyroxenites than in the peridotites, even if the correlation values to S are relatively low (0.46–0.72 R^2). Furthermore, the nearly homogenous composition of Se throughout all the studied rocks (from 0.2 to 3.7 ppm) and the high S contents of the pyroxenites result in variable S/Se ratios, with average values of 148 ± 164 (1SD; n = 20) and 897 ± 761 (1SD; n = 8), for peridotites and pyroxenites, respectively. Molybdenum and As display an opposite trend and are prone to have higher concentrations in peridotites (0.21 ± 0.15 and 1.6 ± 0.8 ppm; 1SD, n = 20) than in pyroxenites (0.15 ± 0.07 and 1.3 ± 0.2 ppm; 1SD, n = 8).

Notably, the distinction of the studied transects into different sectors might be biased due to the sample cutting and the heterogeneity of rock samples. Hence, comprehensive and simultaneous *in-situ* petrological observations (Section 4.2) are crucial for assessing sulfide fertilization quantitatively. Here, in all cases, the whole-rock metal contents follow the microscopy-based sulfide content calculations (correlation between Fig. 4b and g), highlighting the high quality of the conducted analysis.

4.4. *Sulfide compositions*

The sulfides were analyzed for major elements throughout the studied transects (15 thin sections with a total of ~ 1580 analyses) (Table S6). Most Fe-rich sulfide phases are classified as pyrrhotite, approaching a troilitic composition (FeS; inferred for > 62.5 wt% of Fe; n = 406) with several examples (e.g., TS25 and 26) having Fe content of < 61.7 wt% and metal/S ratio of 0.97–0.98. Whereas the Ni content in Fe-rich pyrrhotite is homogenous and low (≤0.10 wt%), the pyrrhotite with relatively low Fe has variable Ni (0.02–0.69 wt%, n = 57). Chalcopyrite is, on average, composed of 34.5 ± 0.3 wt% S, 34.0 ± 0.9 wt% Cu, and 30.4 ± 0.8 wt% Fe, consistently displaying stoichiometric Cu/(Cu + Fe) ratios of 0.50 ± 0.01 (1SD; n = 375). *In-situ* measurements also revealed the occurrence of stoichiometric cubanite within 9 thin sections containing an average 40.4 wt% Fe and 23.4 wt% Cu providing a Cu/(Cu + Fe) ratio of 0.34. Moreover, only one grain (two analytical spots) of bornite Cu_5FeS_4 was measured and gave a Cu content of 58.8 wt % and a Metal/S ratio of 1.37. Pentlandite has a metal/S ratio between 1.05 and 1.14 with an average value of 1.11 ± 0.01 (1SD, n = 750), close to the stoichiometric formula of Me_9S_8. The Co content of pentlandite is low in peridotites and Cr-diopside pyroxenite dykes (<0.7 wt%), whereas it is higher in Al-augite pyroxenite dykes providing average values of 1.7 (TS26) and 4.0 wt% (TS70). The Ni/(Ni + Fe) ratio of pentlandite is 0.43 ± 0.02 (1SD; n = 750).

4.5. *Sulfur speciation and isotope system in sulfides*

Sulfur extracted from the studied samples was generally bound as sulfide-S and exhibited variable concentrations depending on lithology (Table S5). In general, peridotites have low sulfide-S content ranging from 14 to 220 ppm (average value of 138 ppm; n = 19), with one extremely low content of 1 ppm and one higher of 394 ppm measured for a wall rock peridotite. In contrast, pyroxenites are rich in sulfide-S, displaying concentrations of 325 to 1726 ppm with an average of 849 (n = 8). We did not observe any difference between different suites of pyroxenites. These sulfide-S concentrations are in good agreement with total sulfur (TS) contents (ratio > 90 %) for 16 of 27 analyzed samples.

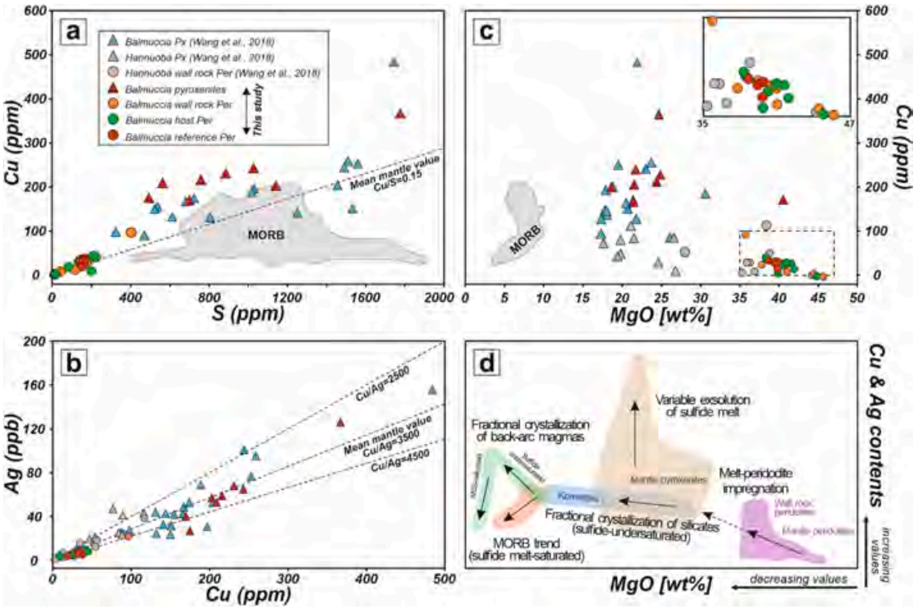

Fig. 3. Harker diagrams illustrating the correlations between contents of a selected elements in the Balmuccia peridotites and pyroxenites. (a-b) Copper vs. S and Ag contents providing positive correlations (R^2 of 0.96 and 0.98, respectively). The reference data for MORBs are from Jenner and O'Neill (2012) and Jenner et al. (2012). (c) Copper content as a function of MgO contents in the Balmuccia mantle peridotites and pyroxenites. The dashed box is enlarged at the top right inset. (d) Corresponding schematic diagram depicting the behavior of Cu and Ag in variable magmatic rocks and processes in relation to their MgO contents. Modified from Wang et al. (2018a).

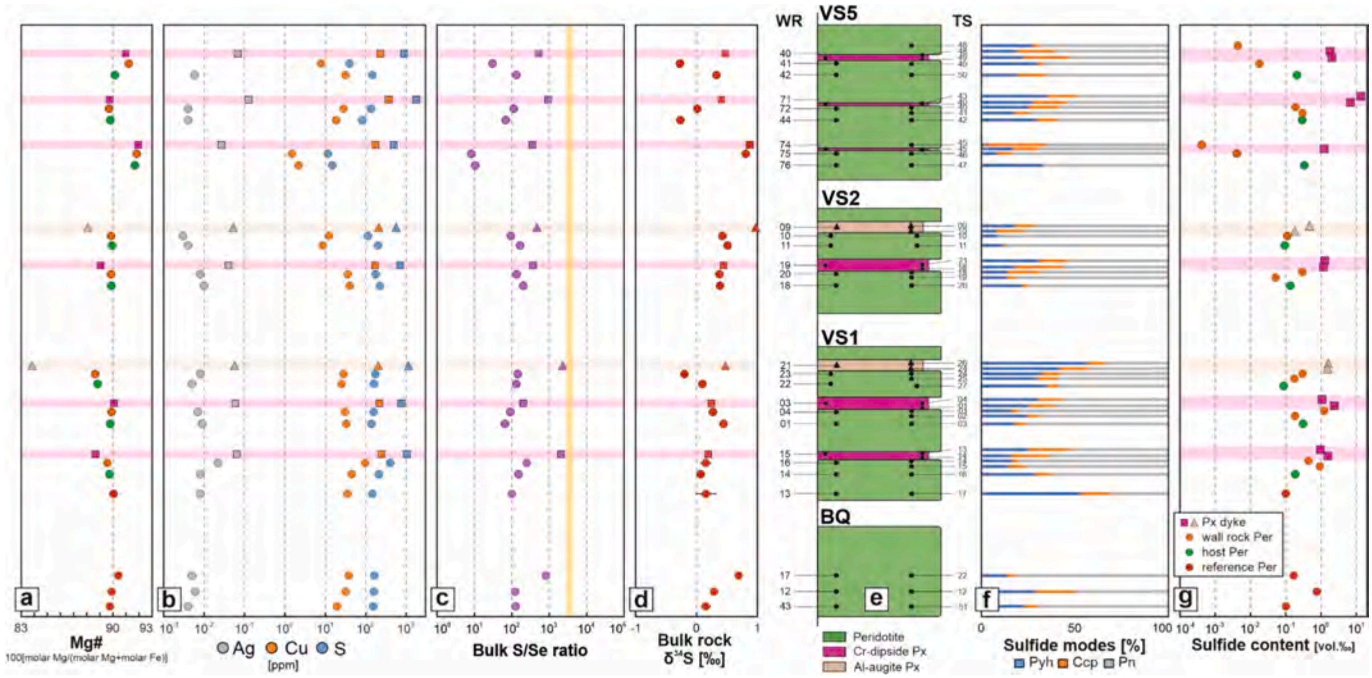

Fig. 4. Summary plots displaying samples lithology, distribution, and selected compositional characteristics throughout the collected transect. (a-d) Compilation of the whole rock-based results including Mg# (a), selected chalcophile elements (Ag, Cu) and S concentrations (b), bulk S/Se ratio (c), and bulk δ^{34}S signatures (d); (e) a simplified lithological profile presenting the distribution of the studied samples including ultramafic dykes with their wall rock and host peridotites and reference peridotites from the Balmuccia quarry. (f) The corresponding sulfide modes and their contents (g) within studied thin sections. Note that sulfide contents correlate with bulk S/Se ratio as well as Cu as and Ag contents. The horizontal boxes through all panels mark the position of the studied pyroxenite dykes. Violet boxes refer to Cr-diopside pyroxenite suite, whereas the beige boxes refer to Al-augite pyroxenite suite. The yellow box in panel c refers to the mantle range of S/Se ratios (Hattori et al., 2002). The error bars in panel d refer to the standard deviation values. The precise locations of sampling sites are provided in Fig. 1. Numbers on both sides of the profile refers to whole rock (WR) and thin section (TS) analyses.

However, we observed that S-poor samples have a lower TS/sulfide-S ratio (Table S5), indicating a low amount and heterogeneous distribution of sulfides within the studied rock (for TS measurements, a small amount of rock powder is measured compared to the extraction of sulfide-S). The sulfate extraction did not reveal any S content in the samples. The S isotopes were determined as total bulk sulfide-S and, separately, as AVS-S and CRS-S. The contribution in sulfide-S of AVS-S and CRS-S differ between samples, with no systematic variations depending on sulfide modes. The bulk rock sulfide-S δ^{34}S range from –0.27 to 0.97 ‰ throughout the entire set of the studied samples without any systematic differences between various rock types (Table S5, Fig. 4). Notably, the CRS-S-derived δ^{34}S have positive values (+0.18 to + 1.96 ‰), being in contrast to AVS-S-derived δ^{34}S, which provides negative values (–1.21 to –0.12 ‰) with one positive value of + 0.35 ‰ (Table S4).

The aforementioned whole-rock δ^{34}S results obtained utilizing the sulfur extraction are supplemented by *in-situ* SHRIMP measurements (n = 168) that have been performed for all sulfide phases identified within the separated polyphase sulfide grains (Fig. 5 and Table S7). Generally, for all sulfide grains in which pyrrhotite co-occurs with other sulfides, either pentlandite or chalcopyrite or both, it has higher δ^{34}S than other phases. The entire interval of δ^{34}S measured for pyrrhotite span from –2.26 to + 1.39 ‰ (n = 18). Notably, we found two pyrite grains in the Al-augite pyroxenite dyke VS1 (TS 24 and 26), which provided the highest δ^{34}S values (+1.61 and + 4.69 ‰). As pyrrhotite is a minor phase in peridotites and wall rock pyroxenites, sulfide grains in these rocks predominantly comprise pentlandite and chalcopyrite. For 7 out of 8 investigated grains, pentlandite displays higher δ^{34}S values than chalcopyrite, ranging from –2.04 to + 1.02 ‰ (n = 86) and from –3.88 to + 0.50 ‰ (n = 60), respectively. In only one sample (TS04), this trend is reversed. In most cases, the standard deviation calculated for multiple measurements of the same sulfide phase is < 0.5 ‰ (17 out of 25 measured sulfides), indicating a relatively homogenous δ^{34}S composition of the individual sulfide phases (Table S7). Based on sulfide modes observed under the reflected light and BSE images, the weighted bulk sulfide δ^{34}S range from –1.55 to + 0.58 ‰ for the polyphase individual sulfide grains (Fig. 5).

4.6. Iron isotopic composition of sulfides

The Fe isotopes of different sulfide phases were measured within both the peridotites and the pyroxenite dykes (Fig. 6, Table S8). Pyrrhotite revealed consistently negative δ^{56}Fe values ranging from –1.44 to –0.36 ‰, with an average value of –0.95 ‰ (n = 13) and broadly similar average δ^{56}Fe signature for peridotites and pyroxenites (–1.25 ‰ and –0.82 ‰, respectively). Chalcopyrite display positive δ^{56}Fe signatures ranging from + 0.13 to + 0.99 ‰, with an average value of + 0.42 ‰ (n = 17). As for pyrrhotite, there is no difference in δ^{56}Fe between different lithologies. Namely, chalcopyrite has an average value of + 0.32 ‰ for peridotites (n = 7) and + 0.49 ‰ for pyroxenites (n = 10). Pentlandite show a similar range of δ^{56}Fe values as chalcopyrite (from –0.33 to + 1.45 ‰) with an average value of + 0.52 ‰ (n = 17). Considering different lithologies, the measured pentlandite within Al-augite pyroxenites have higher δ^{56}Fe values with an average of + 0.86 ‰ compared to the remaining pentlandites (Table S8). Based on mass balance calculations for polyphase sulfide grains (n = 10), for which all the identified sulfide phases were measured, the bulk sulfide δ^{56}Fe signatures in peridotites and pyroxenites from Balmuccia massif range from –0.40 ‰ to + 0.50 ‰ (Fig. 6).

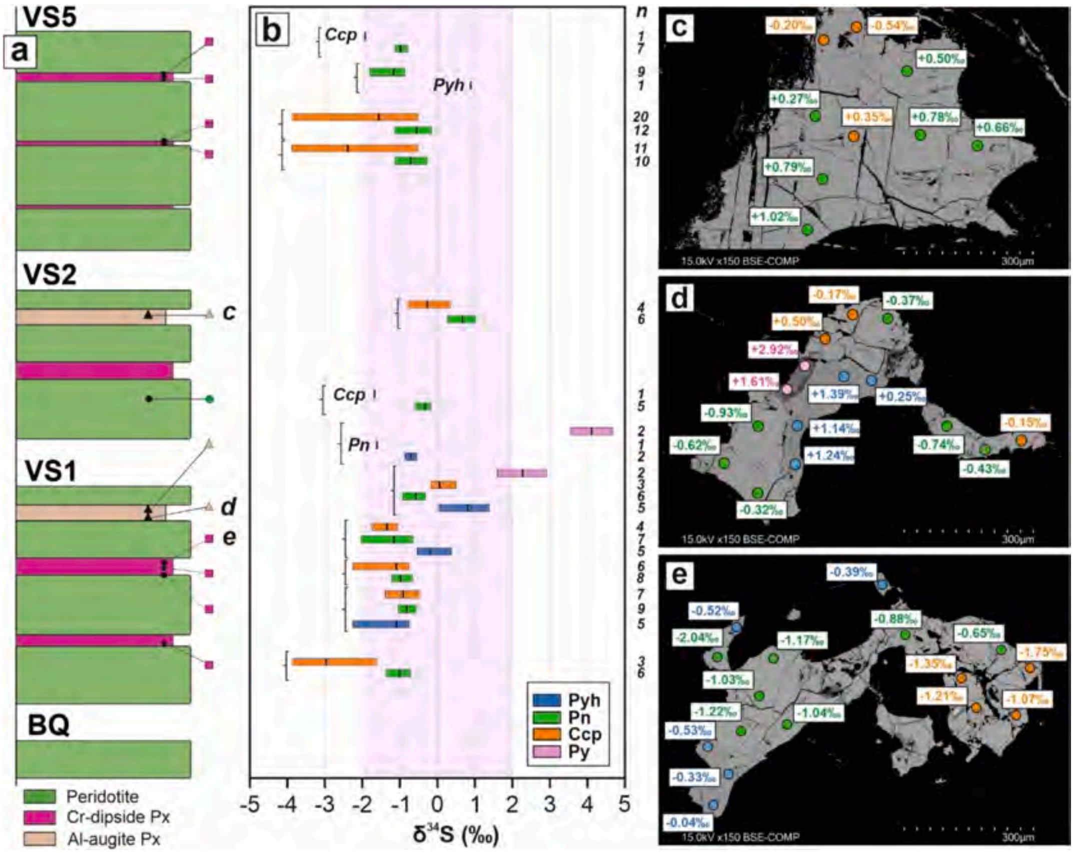

Fig. 5. Compilation of the $\delta^{34}S$ signatures obtained for the ultramafic dykes within the Balmuccia massif. (a) Schematic lithological profile with locations of selected samples for SHRIMP/Ile measurements. (b) Boxplot of the $\delta^{34}S$ signatures determined for all sulfide phases identified in a specific sample. The light violet band represents mantle's S isotopic composition considered 0 ± 2 ‰ (Seal, 2006). n – number of analytical points. (c-e) Examples of separated sulfide grains under BSE images with locations (dots) of analytical points and corresponding $\delta^{34}S$ values. The colors of the points correspond to the boxplots. The locations of the samples are pointed by letters on the lithological profile.

5. Discussion

5.1. Sulfide mineralization in Balmuccia pyroxenites

The Balmuccia mantle pyroxenites were most likely formed by mantle-derived melts exhibiting variation between OIB and MORB affinities, which migrated within the upper mantle, leading to its refertilization (Shervais and Mukasa, 1991; Rivalenti et al., 1995; Mukasa and Shervais, 1999; Wang and Becker, 2015b; Ogunyele et al., 2024). Although the pyroxenite-forming melts differed in composition and temporal evolution, the primary mantle magmas originated from an isotopically similar source region. These rocks have similar Nd-Sr isotopic signatures (Sinigoi et al., 1983; Shervais and Mukasa, 1991; Rivalenti et al., 1995; Mukasa and Shervais, 1999) and our sulfide-based studies have shown that these dykes share coherent sulfide characteristics. These include comparable metal contents, sulfides mineralogy (increased contribution of Pyh and Ccp in pyroxenites), abundance (sulfide enrichment), and sulfide geochemistry (homogenous chemical composition of sulfides) (Fig. 4). Despite these observations, Wang and Becker (2015b) reported these two suites of pyroxenites differ in the contents and ratios of chalcophiles and the highly siderophile elements. This difference is likely caused by varied sulfide segregation and sulfide melt-silicate melt partitioning during magmatic evolution and interaction between the melts and peridotite in the mantle (Wang and Becker, 2015b). The adjacent mantle peridotites revealed relatively homogenous sulfide contribution and mineralogy, however, distinctive from the Balmuccia pyroxenites. In the present study, despite some differences between the pyroxenite suites, we considered the Cr-diopside pyroxenites and the Al-augite pyroxenites together to provide insights into the upper mantle metallogeny.

The subcontinental mantle P-T conditions (spinel facies) at the time of pyroxenite formation enabled the melt-peridotite reaction and segregation of the primary magmatic sulfide liquid. This liquid subsequently crystallized to monosulfide solid solution (MSS) and intermediate solid solution (ISS), which then recrystallized into low-temperature (<650 °C) sulfide assemblages (Holwell and McDonald, 2010; Helmy et al., 2021; Mansur et al., 2021). Distinct sulfide phases (pentlandite-pyrrhotite-chalcopyrite; Fig. 2d-g) exsolved from the MSS and ISS upon cooling under stable conditions, and their recrystallization was followed by subsolidus equilibration. The contribution of pentlandite in peridotite decreases towards the dykes, as the pyrrhotite-chalcopyrite assemblages are abundant in the pyroxenites (Fig. 4e). This observation can be explained by the increased Ni content in the mantle rocks, causing the MSS to be enriched in Ni and thus prone to pentlandite crystallization. To some extent, the wall rock peridotites, affected by the pyroxenite-forming percolating melts, display higher contents of pyrrhotite and chalcopyrite, compared to the host peridotites (Fig. 4). The predominantly interstitial and enclosed textural positions of sulfides present both in the pyroxenites and peridotites, as well as the same bulk composition of sulfides in both textural positions provide evidence that the mantle-derived melts were supersaturated in sulfides early upon the emplacement (Garuti et al., 1984; Patten et al., 2013; Holwell et al., 2022). This inference is supported by the S/Se ratios and S isotopic signatures of the pyroxenite dykes that are close to or within the mantle values (Fig. 4) (Hattori et al., 2002), rejecting the involvement of assimilated crustal material.

Cherdantseva et al. (2024b) suggested that volatile-rich phases originating from carbonate melts could have facilitated enhanced sulfide

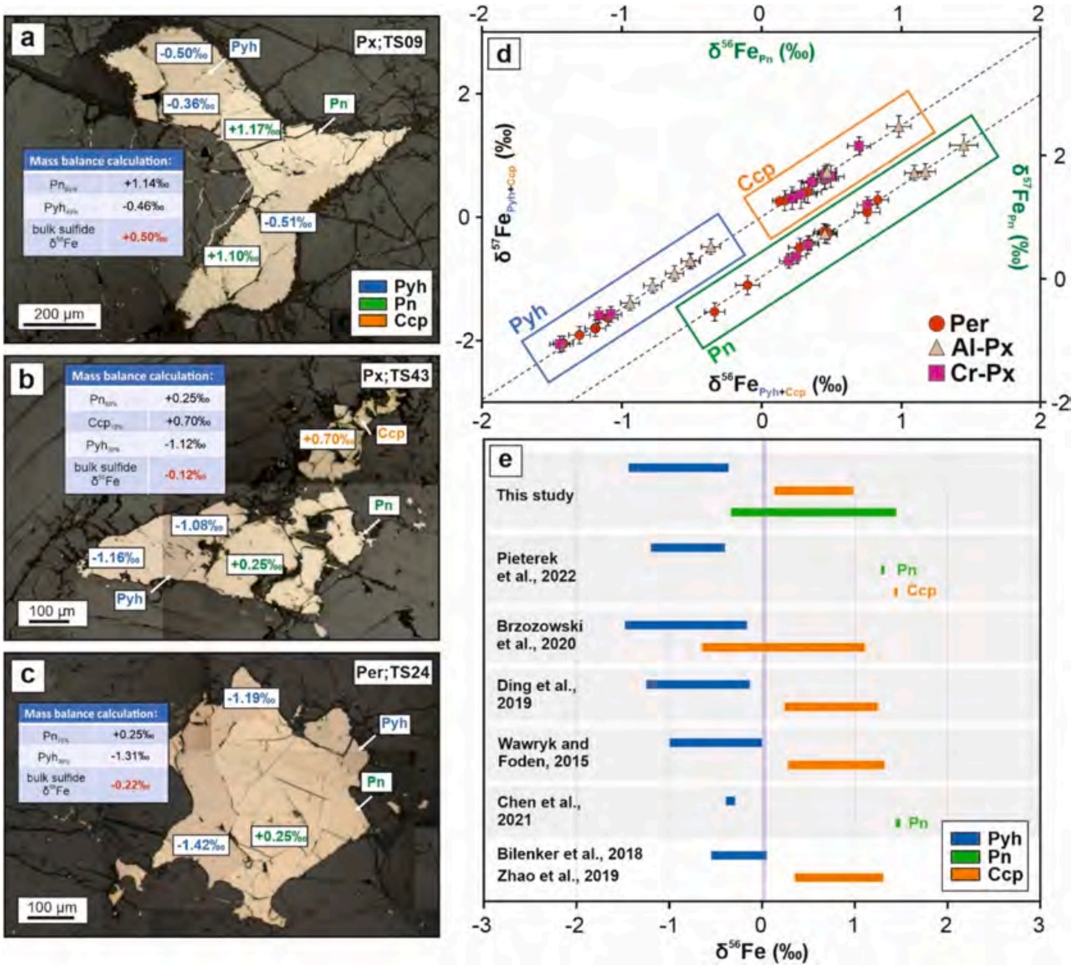

Fig. 6. Summary of the δ^{56}Fe signatures determined for sulfide phases in the ultramafic dykes within the Balmuccia massif. (a-c) Reflected light images of the polyphase sulfide grains with approximated locations of measurement points and their corresponding δ^{56}Fe values. The insets report the mass balance calculations of the bulk sulfide δ^{56}Fe signature based on the sulfide assemblage contribution. The thin section (TS) number is provided in the right top inset and refers to the lithological profile in Fig. 4. Px – pyroxenite; Per – peridotite. (d) Compilation of the δ^{56}Fe signatures obtained for different sulfide phases. The δ^{56}Fe values for pyrrhotite (Pyh) and chalcopyrite (Ccp) are scaled to the same axis, whereas pentlandite (Pn) results are shifted for better visualization. (e) Comparison of the δ^{56}Fe signatures from this and other studies. The light violet band represents the average Fe isotopic composition (δ^{56}Fe) of the terrestrial mantle $\delta^{56}\text{Fe}=+0.025 \pm 0.025$ ‰ (Weyer and Ionov, 2007; Craddock et al., 2013).

transport in magmatic processes. Hydrous minerals (e.g., phlogopite and amphiboles) can also concentrate, for instance, Ni or Cu, effectively controlling the metal flux (Farquhar et al., 1996; Ezad et al., 2024a). The negligible occurrence of hydrous phases, such as amphibole, in both Cr-diopside and Al-augite pyroxenite suites, along with the absence of carbonate minerals, strongly suggests that sulfide transport occurred independently of volatile-rich or carbonate melts. This interpretation is further supported by the major and trace element compositions observed across the pyroxenite suites, which reflect mantle-derived melt processes with localized melt-peridotite interaction and sulfide segregation. Additionally, the S and Fe isotopic signatures of sulfides from both suites exhibit values consistent with mantle-derived processes, further reinforcing the conclusion that metasomatism driven by volatile-rich or carbonate melts did not play a significant role in the formation of these dykes or associated sulfide enrichment.

On the other hand, as evidenced by an experimental study (Wang et al., 2023), the melt flow velocity within the melt-rock reaction zones is potentially high enough to drive sulfide droplets upwards. The higher the melt flow and wider high-degree melt-rock reaction zones, the larger the sulfide droplets are, and the more prone they are to be transported, fertilizing the lithospheric mantle. Considering the lack of covert agents promoting extended vertical sulfide transport (Cherdantseva et al., 2024a) within the crystal mush, we asserted that sulfide migration was likely limited only to the subcontinental lithospheric mantle and not further into the lower crust.

We reported the presence of negligible amounts of secondary sulfides such as pyrite and bornite (Table S6). This observation aligns with the sulfide mineralogy described by Garuti et al. (1984) for the Balmuccia peridotites. We found these sulfides in both lithologies, which are more abundant in the pyroxenites. Since these phases occur at the rims of the primary sulfide grains, we mostly agree with Garuti et al. (1984) that they were likely formed by the replacement and/or remobilization of preexisting sulfide phases. Considering that these sulfide phases crystallize at low temperatures, they were likely caused by shallow-depth or near-surface alteration of the Balmuccia massif. Due to their small amount and secondary origin, they were not considered in this study as they do not contribute to the upper mantle metallogeny. In addition, we also found cubanite crystals that might have exsolved from ISS below 210 °C (Mansur et al., 2021) or, in case of strong alteration which is not the case here, represent the product of chalcopyrite replacement (Djon and Barnes, 2012). Overall, the Balmuccia mantle rocks record pristine sulfide mineralization, offering valuable insights into the undisturbed mantle metallogeny.

5.2. *Refertilization of wall rock peridotites*

The mantle-derived focused melts migrating throughout the subcontinental lithospheric mantle likely interact with the hosting peridotites (Fig. 2a-c). This results in the reactive percolation of the melts into the wall rock peridotites and their refertilization (Lorand, 1989a; Mazzucchelli et al., 2009; Borghini et al., 2020; Belousov et al., 2021; Borghini et al., 2022). This process in Balmuccia is traced by the lowering of Mg# and Cr# in pyroxenes and spinels in peridotites at the contact with pyroxenites (Mukasa and Shervais, 1999).

Based on the Balmuccia pyroxenites, Wang and Becker (2015b) inferred that dissolved sulfides from the mantle peridotites may be transported by percolating melts and subsequently precipitated, leading to the refertilization of peridotites elsewhere in the mantle. Here, utilizing a detailed investigation of sulfides, we tracked the behavior of sulfides at the interface between pyroxenites and peridotites, and quantitatively defined the extent of sulfide fertilization into wall rock peridotites (Fig. 7a). We observed a decreasing content of sulfides from pyroxenites to host peridotites (Fig. 4). This trend is supported by the whole rock geochemical analyses documenting that some of the wall rock peridotites (4-cm-thick zone) have higher Cu, Ag, and S contents (Fig. 3c and 4). Similar to our study, peridotites interbedded with pyroxenite layered series in the eastern Pyrenean peridotites reveal higher Cu and S content with respect to reference massive peridotites (Lorand, 1989a). However, this trend is not always observed for the Balmuccia pyroxenite-peridotite association (Figs. 4 and 7). In particular, for thin pyroxenite dykes (site VS5) we found that the wall rock peridotite samples are depleted in sulfides with respect to both the dykes and host

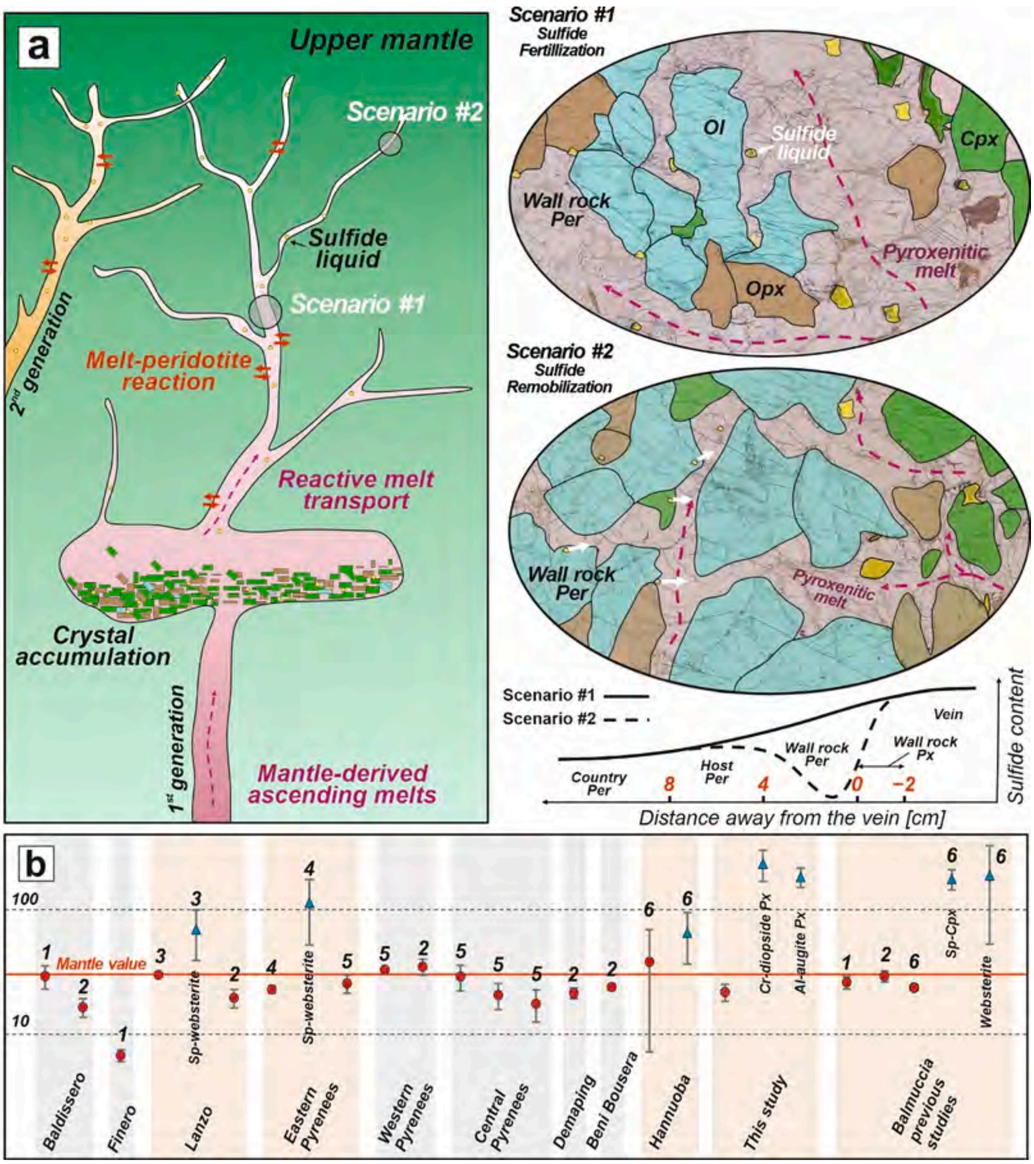

Fig. 7. Contribution of mantle pyroxenites to the upper mantle metallogeny. (a) Schematic illustration showing the distribution of pyroxenite dykes within the upper mantle with a two-scenario model of sulfide behavior during the melt-peridotite reaction (for more discussion see section 5.2). Depending on the dyke thickness, the wall rock peridotite might have been refertilized by the percolating melts causing sulfide precipitation and thus, sulfide and chalcophile enrichment. In contrast, thin dykes (∼1 cm) highlighted by the sharp interface and reaction zone (Cr-diopside or dunite) most likely remobilized sulfides and incorporated them into the upward migrating melts. (b) Compilation of the Cu content from various peridotite massifs and xenoliths in comparison with Cu content of mantle pyroxenites from Lanzo, Eastern Pyrenees, Hannuoba, and Balmuccia. The error bars refer to 1SD. The grey boxes refer to the same massif, whereas the orange boxes highlight locations for where Cu content has been determined for both lithologies. The reference value of Cu content for the mantle is from (McDonough and Sun, 1995), whereas numbers above the symbols refer to: 1 – Garuti et al., 1984; 2 – Wang and Becker, 2015a; 3 – Lorand et al., 1993; 4 – Lorand, 1989a; 5 – Lorand et al., 1999; 6 – Wang et al., 2018a.

peridotites. This observation supports the notion that peridotite-hosted sulfides might have been dissolved and remobilized due to the melt-peridotite reaction (Fig. 7a) (Wang and Becker, 2015b). This is in agreement with the experimental study of Wang et al. (2023), who showed that with the increasing melt-peridotite reaction degree, dense sulfide droplets can be easily transported upwards. In addition, Ezad et al. (2024) and Blanks et al. (2025) demonstrated that the melting of hydrous peridotites may occur at lower temperatures compared to dry peridotites, controlling the metals flux and their distribution at the melt-peridotite interface. The same trend for Cu content, as in our study, was also reported by Lorand (1989b), who found a decreased Cu content for wall rock peridotites of amphibole-rich dykes. These studies show that migrating pyroxenite melts, either hydrous or not, likely affect and control the sulfide and metal distribution in the enclosing peridotites.

In the present study, a relatively low Cu content in the wall rock peridotite was only observed for the thin (~1 cm thick) Cr-diopside websterite dykes in the VS5 sampling site. Hence, we propose that the thickness of the pyroxenite dyke controlled the products and the extent of melt-peridotite reactions and, therefore, the distribution of sulfides. Namely, the thick pyroxenite dykes reveal a broad reaction zone with the enclosing peridotites, which are thus refertilized with sulfides (scenario #1; Fig. 7a). The slow cooling of the thick dykes resulted in a prolonged melt-peridotite interaction, which allowed the sulfide-rich, pyroxenite-forming melts to percolate into and through the wall rock peridotite. In contrast (scenario #2), the fast cooling of the thin (~1 cm) dykes caused the interstitial sulfides hosted by wall rock peridotite, which are prone to melting and further remobilization compared to silicates, to be dissolved and incorporated into the migrating melts (Fig. 7a). Although our results allow us to infer the described scenarios, the variety and heterogeneity of pyroxenite dykes hosted by Balmuccia massif indicate that to constrain the refertilization process of enclosing peridotites a dedicated study is needed.

Our observations point out the complexity of sulfide distribution controlled by the pyroxenite dykes in the upper mantle. Although the formation of pyroxenite dykes was associated with the segregation of sulfides and refertilization of wall rock peridotites, the same generation of pyroxenite-forming melts could have remobilized the restitic sulfides enhancing the sulfide contents in the migrating melts.

5.3. *Isotope fractionation in sulfides*

5.3.1. *S isotope system*

Although the within-sample distribution of sulfides in the Balmuccia peridotite massif is heterogenous (Garuti et al., 1984; Wang and Becker, 2015a; Wang and Becker, 2015b; Zou et al., 2019), the ratio between the TS and extracted Sulfide-S contents, especially for the S-rich pyroxenites, are mostly > 90 %, with almost all samples > 75 %, and with three exceptionally low ratios for the samples characterized by the lowest amount of S (Table S5). Indeed, some of the discrepancies could be caused by incomplete combustion of sulfate-S in the furnace or from incomplete extraction of sulfur during the sequential wet chemical extraction procedure (Oeser et al., 2012). However, our results demonstrate that S is primarily incorporated into sulfides, which aligns with the minimal alteration of the studied rocks. For all the pyroxenites, we conducted the S extraction both by AVS and CRS methods, which revealed CRS δ^{34}S invariably higher than AVS δ^{34}S. Theoretically, AVS is related to monosulfide phases such as, for example, pyrrhotite, whereas CRS includes disulfide phases such as chalcopyrite and pyrite (Oeser et al., 2012). The difference between the AVS and CRS δ^{34}S values ($\Delta^{34}S_{AVS-CRS}$) ranges from + 0.52 to + 2.12, indicating S isotope fractionation between sulfide phases. Considering the total δ^{34}S values, we observed no trends along the studied transects or between the lithologies. The total δ^{34}S overall ranges from –0.27 to 0.97 ‰, being in the interval of mantle-derived S (0 ± 2 ‰; Ripley and Li, 2003; Seal, 2006; Shanks, 2013) and therefore suggesting a pristine mantle origin for the pyroxenite-forming melts. Besides the mantle-hosted dykes, the δ^{34}S signature of ultramafic rock bodies (called pipes) in the adjacent Mafic Complex similarly reveals nearly homogeneous compositions, with values close to zero (+0.04 to + 2.1 ‰) (Garuti et al., 1986; Garuti et al., 2001).

To provide in-depth insights into the S isotope fingerprint of the different sulfide phases, we examined sulfide grains cut out from the same samples for which whole-rock sulfur extraction and isotopic measurements were performed. The natural S isotope variability among magmatic sulfide phases has already been highlighted by *in-situ* measurements (Li and Liu, 2006; Seal, 2006; LaFlamme et al., 2016). The theoretical calculations of the S isotope fractionation over the temperature range from 1000 °C to crystallization indicated ^{34}S enrichment in pyrrhotite compared to chalcopyrite (Li and Liu, 2006). The theoretical considerations are consistent with our results, as pyrrhotite invariably has higher δ^{34}S than the other magmatic sulfide phases. Notably, the analyzed polyphase sulfide grains are Ni-rich, predominantly containing pentlandite, and we typically observed that the δ^{34}S of pentlandite is higher than that of chalcopyrite and lower than that of pyrrhotite (Fig. 5). The observed trend is consistent with the results obtained for similar multiphase sulfide grains of Long-Victor nickel-sulfide deposit, for which the fractionation was related to the natural affinity of ^{34}S to pyrrhotite over pentlandite (LaFlamme et al., 2016). In the case of sulfide grains in which pentlandite coexists with pyrrhotite, the δ^{34}S difference between these phases ranges from 0.3 to 1.4 ‰, with one exceptionally high value of 2.1 ‰ (Table S7). The calculated $\Delta^{34}S_{pyrrhotite\text{-}pentlandite}$ is located in previously proposed range of 0.7–1.0 ± 0.5 ‰ (LaFlamme et al., 2016) and supported by the results (variability of < 0.5 ‰) provided for the ultramafic rock bodies in the adjacent Mafic Complex (Fiorentini et al., 2018). Considering the δ^{34}S difference between coexisting pyrrhotite and chalcopyrite in selected samples, the Δ^{34}S ranges from 0.2 to 1.1 ‰. The calculated values of S isotope fractionation between pyrrhotite and chalcopyrite is only 0.4 ‰ at 650 °C (Li and Liu, 2006), a temperature of ISS recrystallization. Although the observed δ^{34}S fractionation exceeds the theoretical values, a difference of 3.6 ‰ was also reported in magmatic sulfides of the lower oceanic crust (Pieterek et al., 2022). These results indicate that S isotopic equilibrium was not maintained during (re)crystallization of sulfide liquid. Subsequently, the S isotope composition might have been disturbed by kinetic fractionation effects related to mass-dependent fractionation processes and S diffusion between the sulfide phases upon subsolidus (re)crystallization (Seal, 2006). Furthermore, the δ^{34}S can depend on the relative proportions of sulfide phases being in equilibrium in the studied sulfide grain. However, such inference can be biased by the two-dimensional nature of the conducted analyses.

Besides the typical magmatic assemblages with negligible amounts of secondary sulfides, the selected grains for SHRIMP measurements revealed the presence of small (~50 μm) pyrite grains (Fig. 5d). Pyrite provided δ^{34}S values that are typically at variance compared to those of the other sulfides of clear magmatic origin. Indeed, pyrite occurs at the margin of polyphase sulfide grains, indicating an origin by replacing magmatic sulfides. The δ^{34}S signature of pyrite is beyond the mantle range (Seal, 2006), with δ^{34}S values similar to those of sulfides from crustally contaminated ultramafic bodies at the base of the adjacent Mafic Complex (Fiorentini et al., 2018). Some ultramafic rocks locally provided high δ^{34}S (>5.0 ‰) of the pentlandite and pyrrhotite, suggesting the input of crustal contamination during the magmatic ore-forming processes. Therefore, the δ^{34}S of pyrite could reveal an interaction between fluids derived from S-bearing crustal rocks and magmatic sulfides initially present in the mantle. Interestingly, the comparison between the δ^{34}S determined for different sulfide phases and whole-rock δ^{34}S determined as AVS and CRS question the current inference about the affinity of AVS to monosulfide phases and consequently CRS to disulfide phases (Oeser et al., 2012). For instance, chalcopyrite, which is disulfide, shows mainly negative δ^{34}S signatures (from –3.88 to + 0.50 ‰), whereas the $\delta^{34}S_{CRS}$ values are positive (+0.18 to + 1.96 ‰). The whole-rock $\delta^{34}S_{CRS}$ can be partially balanced by positive $\delta^{34}S$ signatures of pyrite (+1.61 and + 4.69 ‰). However, the contribution of secondary sulfides in the studied samples is almost negligible. The *in-situ* $\delta^{34}S$ values of monosulfide phases (pyrrhotite and pentlandite) align with the range of $\delta^{34}S_{AVS}$ results. Altogether, our results support the persistent need for detailed analyses when small deviations of isotopic signatures are derived from the bulk rock analyses (Bekker et al., 2009; LaFlamme et al., 2016).

5.3.2. Fe isotope system

Iron isotopes constitute one of the novel geochemical tools helpful in characterizing the sulfide formation processes in the Balmuccia rocks. The presence of large, polyphasic magmatic sulfide grains with minimal alteration enabled us to study the $\delta^{56}Fe$ signatures in different sulfide phases, offering new insights into Fe isotope fractionation under subcontinental lithospheric conditions. Brzozowski et al. (2021) and Ding et al. (2019) documented opposite $\delta^{56}Fe$ values for coexisting sulfides. Namely, negative signatures for pyrrhotite (median value of –0.61 ‰ and –0.49 ‰, respectively) and positive for chalcopyrite (median value of + 0.30 ‰ and 0.96 ‰) (Fig. 6). This trend was also observed by Wawryk and Foden (2015), who measured $\delta^{56}Fe$ signatures of sulfides in magmatic-hydrothermal deposits and obtained negative values (from –1.0 ‰ to 0.0 ‰) for pyrrhotite and positive (+0.28 ‰ to + 1.32 ‰) for chalcopyrite. These patterns for $\delta^{56}Fe$ in sulfides align with determinations for single sulfide phases (Bilenker et al., 2018; Zhao et al., 2019), indicating fractionation between different sulfide phases. Moreover, Brzozowski et al. (2021) highlighted that the large variability of isotope signatures among sulfide phases may be best explained by equilibrium isotope fractionation between the sulfide phases and their relative portions in the samples.

The inherent segregated sulfide grains crystallized from an immiscible sulfide liquid, most likely being in equilibrium as base metal sulfides (BMS) upon cooling and subsequent re(crystallization) (Holwell and McDonald, 2010; Mansur et al., 2021). Consequently, the Fe isotopes fractionated among various BMS, with the heavy isotope (^{56}Fe) being preferentially incorporated into the mineral structure with the highest bond stiffness (Schauble, 2004; Brzozowski et al., 2021 and references therein). This resulted in the preferential incorporation of light isotopes (^{54}Fe) into a MSS, which further recrystallized during cooling (650° to 250 °C) to pyrrhotite-pentlandite assemblages. The preferential partitioning of light Fe isotopes into MSS resulted in a residual Cu-rich liquid (which crystallized into a ISS at 900–800 °C) and subsequently to chalcopyrite (650–250 °C) that is enriched in heavy Fe isotopes. This is expressed by the positive $\delta^{56}Fe$ values determined in this study (Fig. 6). As our samples lack MSS, which is fully recrystallized to pyrrhotite-pentlandite or pyrrhotite-pentlandite-(chalcopyrite) assemblages, our constraints can be only established on the final sulfide phases and their modal relationships recorded in thin sections.

Based on the experimental isotope-exchange data (Polyakov and Soultanov, 2011), the Fe β-factor (defined as the equilibrium isotope ratio of the substance of interest relative to the isotope ratio of dissociated atoms) for troilite (iron-rich sulfide as pyrrhotite in our case) should be smaller compared with chalcopyrite resulting in the heavy Fe isotopes concentrated in chalcopyrite (for more detailed discussion see Ding et al., 2019). This is in accordance with our observations as $\delta^{56}Fe$ of pyrrhotite ranges from –1.44 to –0.36 ‰, whereas chalcopyrite displays opposite values from + 0.13 to + 0.99 ‰. Additionally, the extent of Fe isotope fractionation between pyrrhotite and chalcopyrite is reported to be in the range of 1.06–1.77 ‰ (Ding et al., 2019; Zhao et al., 2019; Brzozowski et al., 2021) indicating Fe isotope equilibration in a cooling sulfide liquid may persist at temperatures below 200 °C (Ding et al., 2019). Our results fall within this range of Fe fractionation for the pyrrhotite-chalcopyrite pairs, with values ranging from 0.93 to 2.00 ‰ based on sample $\delta^{56}Fe$ average values (Table S8).

In magmatic sulfides, the amount of pentlandite within sulfide grains remarkably contributes to the Fe isotope fractionation during the recrystallization of MSS. Given that the pentlandites typically occur as small crystals (most often lamellae or flames), especially in the crustal rocks (Ding et al., 2019; Jesus et al., 2020; Pieterek et al., 2022; Pieterek et al., 2024), their $\delta^{56}Fe$ signatures are poorly constrained. For example, due to the measurement limitations and small size of pentlandite crystals, Ding et al. (2019) assumed that the Fe isotopic signature of pentlandite was identical to that of measured pyrrhotite. However, as evidenced by other studies (Bekker et al., 2009; Bilenker et al., 2018), pentlandite is isotopically slightly heavier than pyrrhotite, by 0.06 ± 0.08 ‰ in $\delta^{56}Fe$. The $\delta^{56}Fe$ values of pyrrhotite-pentlandite pairs that recrystallized from MSS were also measured in gabbroic rocks from the lower oceanic crust (Pieterek et al., 2022) and yielded the same opposite $\delta^{56}Fe$ signatures as the pyrrhotite-chalcopyrite (MSS-ISS) pairs (Fig. 6 and Table S8). Chen et al. (2021) also found similar values, reporting negative $\delta^{56}Fe$ values for JC-Po pyrrhotite (–0.34 ± 0.07 ‰; 2SD, n = 9) and positive for JC-Pn pentlandite (+1.47 ± 0.04 ‰; 2SD, n = 4), collected from the Jinchuan Ni–Cu–PGE sulfide deposit (North China Craton). These results indicate that the ongoing subsolidus cooling (650–250 °C) and subsequent recrystallization of MSS caused increasing Fe fractionation between pyrrhotite and pentlandite. This is aligned with the Fe β-factors determined for (Ni,Fe) S solid solution (Liu et al., 2022), which decrease approximately linearly with the increasing Fe content. Considering the lower Fe content in pentlandite (ranging from 33 to 39 wt%) with respect to Fe-rich pyrrhotite (>62 wt%), pentlandite should have a higher Fe β-factor and thus be enriched in heavy Fe isotopes compared to co-existing pyrrhotite, which is confirmed by our results (Fig. 6). In addition to pyroxenite-hosted sulfides, higher $\delta^{56}Fe$ values of pentlandites with respect to pyrrhotite (Fig. 6c) are well detectable in the studied Balmuccia peridotites as the amount of chalcopyrite is lower than in pyroxenites and, therefore, MSS could have retained the parental Fe isotope composition. In these sulfide grains, pentlandite predominates over pyrrhotite, and mostly displays positive $\delta^{56}Fe$ signatures (e.g. TS24; TS15 Table S8) compared to pyrrhotite, thereby compensating the bulk sulfide $\delta^{56}Fe$ values (Fig. 6c).

This study also found some pyroxenite-hosted sulfide grains comprising both pentlandite and chalcopyrite characterized by positive $\delta^{56}Fe$ values (sample TS14). As we may expect that these grains also contain a higher amount of pyrrhotite (observed crystals were too small for measurements) that has not been exposed on the thin section surface, these results seem to be reasonable assuming the co-occurrence of pyrrhotite characterized by negative $\delta^{56}Fe$. In addition to these observations, we measured the $\delta^{56}Fe$ signatures in one peridotite sulfide grain (sample TS15) consisting of pentlandite (~70 %) and chalcopyrite (~30 %) with no evidence for pyrrhotite, which display contrasting values (–0.10 ‰ (n = 1) and on average + 0.32 ‰ (n = 3), respectively). Using the Fe β-factor calculations provided by Liu et al. (2022), the lower Fe content in chalcopyrite (ranging from 29 to 33 wt%) compared to pentlandite should result in a higher Fe β-factor, and consequently, may explain the higher $\delta^{56}Fe$ values observed for chalcopyrite. This indicates that in the case of MSS recrystallization only to pentlandite, the pentlandite likely retains the initial $\delta^{56}Fe$ values provided during MSS-ISS fractionation.

Given that the chalcopyrite as an ISS recrystallization product preferentially incorporates heavy Fe isotopes, thus lowering the $\delta^{56}Fe$ of co-crystallizing MSS, which further recrystallizes to two sulfide phases characterized by opposite $\delta^{56}Fe$, the Fe fractionation between the sulfide grain assemblages is controlled by subsolidus cooling and the modal amount of crystallized the sulfide phases and, therefore, also indirectly by the chemical composition of the segregated sulfide liquid. Additionally, the $\delta^{56}Fe$ values of pyrrhotite could have been affected by low-temperature (<140 °C) exsolutions of troilite, which is isotopically light relative to coexisting metal phases (Williams et al., 2006). Although the troilite exsolutions have been found in the adjacent Contact Series rocks, at the contact between the Balmuccia massif and Mafic Complex (Pieterek et al., 2024), we did not observe any of them based on petrographical observations in the studied samples. However, we cannot exclude their presence, as the homogenous chemical composition of Fe-rich pyrrhotite (metal/S ratio of 0.98–0.99) is close to the stoichiometric composition of troilite. The present study characterizes the Fe isotopic signature of different sulfide phases of clear magmatic origin, documenting the δ^{56}Fe fractionation at various stages of BMS (re)crystallization from segregated sulfide liquid. Despite the distinct δ^{56}Fe values for different sulfide phases, the mass balance calculations indicate a relatively homogenous Fe isotope composition of mantle-derived sulfide liquid (Fig. 6). We thus support the inference that Fe isotopes fractionate at all stages of the sulfide (re)crystallization (Brzozowski et al., 2021). To provide in-depth insights into Fe isotope fractionation among sulfides, the δ^{56}Fe compositions of coexisting silicates and spinel must be addressed which is beyond the scope of this study.

5.4. Role of mantle pyroxenites in the metal transfer

The effective metal transfer throughout the lithospheric mantle and crust is one of the most important factors controlling the formation of the largest mineralizing systems on Earth. The Cu endowment is solely controlled by sulfides (Blanks et al. 2025), whose distribution depends on source composition and degree of mantle melting. Given that the IVZ zone represents one of the best-preserved exposed sections of the lower continental crust section with fresh mantle bodies devoid of any evidence for metasomatism or crustal recycled materials, which has no considerable porphyry ore deposits in the upper crust section, we have an unprecedented opportunity to witness undisturbed, primary sulfide mineralization and metallogeny of the subcontinental lithospheric mantle and lower crust section. Primary mantle melts are considered to contain higher concentrations of Cu (80–120 ppm; (Jenner et al., 2012; Ding and Dasgupta, 2017) than the bulk lower continental crust (26 ppm Cu; Rudnick and Fountain, 1995) and the Earth's mantle (30 ± 5 ppm; McDonough and Sun, 1995). The difference between the Cu content between the source melts and the considered lithospheric sections indicates the crucial role of magmatic differentiation in sulfide segregation and metallogeny (Fig. 7b). To explain the discrepancy in the Cu content between mantle melts and lower continental crust, the formation of deep-rooted sulfide-bearing cumulates was postulated (Lee et al., 2012; Chen et al., 2020; Pieterek et al., 2024). Although these Cu-rich rocks together with unevenly distributed crustal cumulates in the Mafic Complex and overlying Kinzigite Formation (Garuti et al., 1986; Garuti et al., 2001; Locmelis et al., 2016; Fiorentini et al., 2018; Locmelis et al., 2021; Holwell et al., 2022) most likely constitute an important reservoir of metals, their occurrence cannot fully explain the missing Cu content due to their unclear structural relationship and insufficient contribution in the lithospheric sequence. This implies that a remarkable proportion of metals may be trapped and accumulated in the subcontinental lithospheric mantle, thereby not reaching the crustal section (Fig. 7). Therefore, the Balmuccia mantle body together with its pyroxenite dykes constitutes an ideal exposure, defining the Cu metal budget of the upper mantle. It may also highlights the substantial contribution of pyroxenites for metal flux through crust-mantle transition, which was previously overlooked and not accounted for in global metal budget calculations.

Infiltration of the metal-enriched mantle pyroxenites in the upper mantle could have served as a potential source for the younger, Cu-rich domains (called ultramafic pipes) aged at 290–250 Ma and situated in the lower crust of IVZ (Garuti et al., 2001; Locmelis et al., 2016; Fiorentini et al., 2018). The crustal sulfide-bearing domains and our samples reveal a similarity in mantle-derived sulfur isotope compositions, which fall within a narrow range of ~ 0–1 ‰ (Garuti et al., 2001). However, there is no direct evidence linking these crustal Cu-rich domains to the studied mantle pyroxenite dykes. For instance, Garuti et al. (2001) suggested that the crustal pyroxenites were formed by very low-degree melting at the root or core of the subcontinental mantle plume that caused the underplating event in IVZ. In addition, based on the ages of the crustal pyroxenites, Locmelis et al. (2016) proposed a temporal gap between mantle metasomatism and the partial melting that generated the parental melts for the crustal pyroxenites. This implies that metals had to be stored in the subcontinental lithospheric mantle. However, besides these inferences, there is no evidence for Balmuccia pyroxenite dykes to have undergone any partial melting process after their formation and emplacement. As suggested by Locmelis et al. (2016, 2021), the mantle source of the ultramafic pipes could be hydrous in response to a metasomatic process that occurred during the Variscan subduction. The ultramafic pipes are characterized by different Nd-Sr isotopic signatures ($\mathcal{E}_{290\mathrm{Nd}} = -1.9$ to $+3.7$ and $^{87}\mathrm{Sr}/^{86}\mathrm{Sr} = 0.7044$–$0.7063$ (Garuti et al., 2001)) with respect to Balmuccia-type pyroxenites ($\mathcal{E}_{270\mathrm{Nd}} = +5.5$ to $+6.8$ and $^{87}\mathrm{Sr}/^{86}\mathrm{Sr} = 0.7030$–$0.7038$ (Voshage et al., 1988)). These findings, particularly the Nd-Sr isotopic signatures and the nearly anhydrous nature of the Balmuccia-type mantle section strongly refute a genetic link with the ultramafic pipes of the Mafic Complex. Instead, the observed isotopic and geochemical disparities underscore the independent evolution of these systems within the subcontinental lithospheric mantle.

Considering the Balmuccia peridotite massif, the contribution of pyroxenites was estimated as ~ 5 % (Ueda et al., 2020; Decarlis et al., 2023), thereby allowing us to evaluate the metal budget of this massif and to what extent the pyroxenites contribute to the metal inventory of the subcontinental lithospheric mantle (Table 2). The pyroxenites are enriched in sulfides and associated metals, especially Cu and Ag (up to 367 ppm and 126 ppb, respectively), compared to the enclosing peridotites (29 ± 20 ppm Cu; 7 ± 4 ppb Ag), and are therefore expected to substantially contribute to the metal budget of the Balmuccia mantle body (Fig. 7b). For our calculations, we used the average Cu content for Balmuccia peridotites (29 ppm) and enclosed pyroxenites (227 ppm), obtaining that the pyroxenite contribution to the Cu metal budget of the mantle body is 26 % (Table 2, scenario #1). Given that a similar enrichment was reported for the Balmuccia pyroxenites (Wang and Becker, 2015b; Wang and Becker, 2015a; Wang et al., 2018b; Zou et al., 2019), our calculations indicate that almost a quarter of the Cu inventory in the upper mantle can be accumulated within sulfide-bearing mantle pyroxenites. Considering the Ag enrichment of Balmuccia mantle pyroxenites (62 ± 27 ppb), we performed similar calculations (Table 2) finding that they store 29 % of the mantle Ag budget.

Contents of sulfides in pyroxenites and metasomatized peridotites are often higher compared with those in non-metasomatized peridotites (Shaw, 1997; Lee et al., 2012; Wang and Becker, 2015b; Saunders et al., 2016; Ciazela et al., 2017; Ciazela et al., 2018; Patkó et al., 2021; Fang et al., 2024). This disproportion indicates the critical role of migrating, mantle-derived melts in the metallogeny of the subcontinental lithospheric mantle (Fig. 7). This observation matches current isotopic results showing that a high degree of mantle metasomatism promotes the fertilization of primary magmas in metals (Zhao et al., 2024) that might constitute the source for the formation of magmatic Ni-Cu deposits. Hence, the widespread occurrence of sulfide-bearing pyroxenites implies that these rocks must be accounted for in the metal budget of the lithospheric mantle. Specifically, metal contents (i.e., Cu and Ag) in mantle pyroxenites, in most cases, are poorly studied, but the available datasets show that, for example, Pyrenean alkali and garnet pyroxenites contain up to ~ 240 ppm Cu (Lorand, 1989b; Lorand and Luguet, 2016 and references therein). In addition, Lorand et al. (1993) demonstrated that spinel websterite dykes occurring in the Lanzo massif contain, on average, 69 ppm Cu (~2.5 times more than the hosting peridotites). The Cu concentrations reported for pyroxenites contrast with mantle peridotites that show low and relatively consistent Cu content (Fig. 7b) ranging from ~ 7 ppm in Lanzo massif (Garuti et al., 1984) to ~ 35 ppm in Western Pyrenees (Wang and Becker, 2015a). Similarly to Cu contents, in general, peridotites also reveal low concentrations of Ag (~9 ppb) with respect to our pyroxenites (Wang and Becker, 2015a). Currently, the contribution of pyroxenites in the mantle is constrained to range from < 2 % (Petermann and Hirschmann, 2003) to 5 % (Pearson et al., 1993; Bodinier and Godard, 2003; Decarlis et al., 2023) and can locally reach up to 10 % (i.e., in Beni Bousera; Pearson, 1996). Assuming

Table 2
Estimations of the Cu and Ag metal budget in the Balmuccia mantle massif including the contribution of mantle pyroxenites.

		Scenario #1	Scenario #2	Scenario #3	Scenario #4
Upper mantle					
Contribution of peridotites	[%]	95	98	95	90
Contribution of pyroxenites	[%]	5	2	5	10
Average Cu content in pyroxenites	[ppm]	227	227	227	227
Excess Cu content[a]	[ppm]	198	197	197	197
Contribution to the Cu budget[b]	[% x ppm]	990	394	985	1970
	[%]	26.0	11.8	25.7	42.2
Average Cu content in peridotites	[ppm]	29	30	30	30
Contribution to the Cu budget[b]	[% x ppm]	2755	2940	2850	2700
	[%]	74.0	88.2	74.3	57.8
Average Ag content in pyroxenites	[ppb]	62	62	62	62
Excess Ag content	[ppb]	55	53	53	53
Contribution to the Ag budget[b]	[% x ppb]	275	106	265	530
	[%]	29.3	10.7	23.7	39.6
Average Ag content in peridotites	[ppb]	7	9	9	9
Contribution to the Ag budget[b]	[% x ppb]	665	882	855	810
	[%]	70.7	89.3	76.3	60.4

Scenario #1 – calculated accounting Cu and Ag contents obtained for Balmuccia mantle massif in this study.
Scenario #2–4 – calculated accounting reference Cu values for upper mantle (McDonough and Sun, 1995) and Ag content (Wang & Becker, 2015a).

[a] The average Cu content of the Balmuccia pyroxenites minus the average Cu content for the Balmuccia peridotites (e.g., 227 ppm – 29 pm = 198 ppm). Accordingly, it has also been calculated utilizing the average global Cu content in the upper mantle (e.g., 227 ppm – 30 ppm = 197 ppm).

[b] The contribution to the metal budget has been calculated both for the Balmuccia peridotites and pyroxenites. For the Balmuccia mantle peridotites, we have multiplied the contribution of peridotites within the massif and average Cu content (e.g., 95 %× 29 ppm = 2755 % × ppm), while for the Balmuccia mantle pyroxenites the excess content was multiplied with the contribution of pyroxenites within the Balmuccia massif (e.g., 5 % × 198 ppm = 990 % × ppm). Only the excess content is used to estimate the metal contribution of mantle pyroxenites because a portion of Cu in the mantle pyroxenites sequence is the background value (assumed to be an average content in the Balmuccia mantle peridotites). Similarly, the same methodology was adopted for Ag.

the typical character of sulfide- and associated metal-enrichment in mantle pyroxenites at a similar level to the Balmuccia example (Lorand et al., 1993; Sen et al., 2010; Lorand and Luguet, 2016), the budget of the upper mantle for some chalcophile elements such as Cu might have been underestimated (Table 2; scenarios #2–4), in the range of 12 % to 42 % (for 2 % and 10 % pyroxenite contribution, respectively). Similar underestimation values are obtained for Ag. Besides some local exceptions (e.g., Galán et al. (2016) reported higher amounts of sulfides in lherzolites than in harzburgites and websterites for the xenoliths from the Neogene-Quaternary volcanic zone of Catalonia, NE Spain), our estimations highlight a need for comprehensive investigations of mantle massifs to quantitatively constrain the contribution of mantle pyroxenites to the upper mantle metallogeny.

The studied Balmuccia massif represents the fresh mantle body whose eastern external contact is highlighted by the crustal Contact Series rocks (Fig. 1). Given the crust-mantle transition zone documented in Balmuccia can constitute another metal reservoir (Pieterek et al., 2024), the relation between mantle pyroxenites and Contact Series rocks should be discussed in terms of metal contents and their budget. The Balmuccia pyroxenites are genetically unrelated to the adjacent, sulfide-rich Contact Series cumulates. The mantle pyroxenites and the Contact Series rocks represent distinct stages of Balmuccia mantle evolution (Shervais and Mukasa, 1991; Mukasa and Shervais, 1999). The Contact Series rocks most likely crystallized in the early Permian, whereas the pyroxenites represent a melt influx event of late Devonian age (Ogunyele et al., 2024). Considering the sulfide mineralogy and composition between these two different suites, it is evident that sulfides hosted by the Contact Series contain mainly Fe-rich sulfides, whereas pentlandites dominate mantle pyroxenite sulfides. Moreover, Contact Series rocks reveal lower Mg# ranging from 51 to 75 with respect to mantle pyroxenites (83–90) indicating that these rocks crystallized from more evolved melts. Therefore, the melts responsible for the formation of these rocks cannot be related to each other. Despite these considerations, the rocks contain similar enrichment in sulfides and associated metals, for instance, the average Cu content is 227 ppm in the Balmuccia pyroxenites vs. 141 ppm in the Contact Series. This demonstrates that the crystallization of chemically primitive mantle melts (producing cumulates, either within the mantle or at the mantle-crust transition) can be associated with extensive segregation of sulfides affecting the metallogeny of the subcontinental lithospheric mantle. Therefore, comprehensive sulfide-based studies need to be addressed for other mantle peridotite massifs to provide a robust assessment of pyroxenite contribution to metals inventories.

6. Conclusions

We provide evidence for higher contents of sulfides and chalcophile metals (e.g., Cu, Ag) in mantle pyroxenites compared to host Balmuccia mantle peridotites, pointing out that pyroxenite may play a key role regarding the sulfide inventory of the subcontinental lithospheric mantle. The sulfide-based analyses confirm that the pyroxenite-forming melts were sulfide-saturated before their emplacement and could refertilized the adjacent wall rock peridotites. Our results support the evidence of the heterogenous distribution of sulfides and metals in the subcontinental lithospheric mantle section that should be globally addressed.

The spatial relationships between the pyroxenites and adjacent peridotites allowed us to identify two contrasting trends of sulfide distribution, highlighting the impact of melt-peridotite reactions and mantle refertilization on sulfides. Based on sulfide and associated metals distributions, we show that thick (>4 cm) pyroxenite dykes can fertilize the wall rock peridotites in sulfides. Conversely, the thin pyroxenite dykes (≤1 cm) are enveloped by sulfide-depleted layers which record the melting of wall rock peridotite sulfides by reheating and their subsequent remobilization. This evidences complex and heterogeneous sulfide segregation during the migration of sulfide-saturated pyroxenite-forming melts in the subcontinental lithospheric mantle.

We documented and characterized the isotope fractionation among sulfide phases during (re)crystallization of sulfide liquid. We reported that each sulfide phase in polyphase grains has a distinct S and Fe isotopic signature. This isotope fractionation is most likely driven by mass-dependent isotope fractionation cooling, following sulfide (re)crystallization under high-T subsolidus magmatic conditions. The provided isotopic characteristics can aid isotopic studies and the robust assessment of S and Fe isotope fractionations.

Our results demonstrate that the migration of sulfide-bearing pyroxenite dykes affects the sulfide segregation and related metallogeny within the Balmuccia peridotite massif. We calculated that the reported sulfide enrichment contributes to up to 26 % of Cu and Ag of the local scale metals budget. Although the role of mantle pyroxenites has been mostly overlooked and not adequately addressed in previous studies, we assert that they should have been considered in the metals budget calculations of the subcontinental lithospheric mantle. Our estimations based on global-scale extrapolations of mantle pyroxenites contribution in the subcontinental lithospheric mantle highlight that these rocks can incorporate from 12 % to 42 % of the Cu and Ag inventory of the subcontinental lithospheric mantle, thereby providing crucial implications for the global-scale lithospheric metallogeny.

CRediT authorship contribution statement

Bartosz Pieterek: Writing – review & editing, Writing – original draft, Visualization, Validation, Software, Resources, Project administration, Methodology, Investigation, Funding acquisition, Data curation, Conceptualization. **Magdalena Matusiak-Małek:** Software, Methodology, Investigation, Data curation. **Riccardo Tribuzio:** Writing – review & editing, Supervision, Investigation, Conceptualization. **Marina Lazarov:** Writing – review & editing, Methodology, Investigation, Data curation. **Magdalena Pańczyk:** Software, Methodology, Investigation, Data curation. **Harald Strauss:** Writing – review & editing, Supervision, Methodology, Investigation, Conceptualization. **Thomas Kuhn:** Methodology, Investigation, Data curation. **Zbigniew Czupyt:** Methodology, Investigation, Data curation. **Jakub Ciazela:** Writing – review & editing, Supervision, Investigation, Funding acquisition, Conceptualization. **Stefan Weyer:** Writing – review & editing.

Declaration of competing interest

The authors declare that they have no known competing financial interests or personal relationships that could have appeared to influence the work reported in this paper.

Acknowledgements

We thank editors Hassan Helmy and Hailiang Dong for their guidance as well as Marco Fiorentini and two anonymous reviewers for their thorough and insightful comments that significantly improved the overall quality of the manuscript. This research was financed by a grant funded by the National Science Center Poland (No. 2018/31/N/ST10/02146). The Article Publishing Charge has been financed by the "Excellence Initiative - Research University" programs of the University of Wrocław and Adam Mickiewicz University in Poznań. BP was supported by a START scholarship funded by the Foundation for Polish Science and the Ministry of Education and Science publication grant (62.9012.2423.00.0). We acknowledge Dominik Gurba (PIG-NRI) for preparing the mounts and taking BSE images for SHRIMP/Ile analyses. No permissions were required for the sampling campaign.

Appendix A. Supplementary material

Supplementary Material includes additional figures and tables that constitute an extension of the results related to the characteristics of peridotite-pyroxenite contacts and sulfide distribution. Supplementary material to this article can be found online at https://doi.org/10.1016/j.gca.2025.03.007.

Data availability

Data are available through Figshare repository at https://doi.org/10.6084/m9.figshare.27211479.

References

van Acken, D., Becker, H., Walker, R.J., McDonough, W.F., Wombacher, F., Ash, R.D., Piccoli, P.M., 2010. Formation of pyroxenite layers in the Totalp ultramafic massif (Swiss Alps) - Insights from highly siderophile elements and Os isotopes. Geochim. Cosmochim. Acta 74, 661–683.

Basch, V., Rampone, E., Borghini, G., Ferrando, C., Zanetti, A., 2019. Origin of pyroxenites in the oceanic mantle and their implications on the reactive percolation of depleted melts. Contrib. to Mineral. Petrol. 174, 1–25.

Bekker, A., Barley, M.E., Fiorentini, M.L., Rouxel, O.J., Rumble, D., Beresford, S.W., 2009. Atmospheric sulfur in Archean komatiite-hosted nickel deposits. Science 80). 326, 1086–1089.

Belousov, I., Batanova, V., Sobolev, A., Savelieva, G., Danyushevsky, L., Draayers, E., 2021. Pyroxenites from mantle section of Voykar Ophiolite – Melt/peridotite reaction and crystallization in SSZ mantle. Lithos 388–389, 106063.

Beltrando, M., 2021. Can the scale of observation hide complexities in the deformation history of a terrane? An examples from Balmuccia peridotite massif, Ivrea Zone (NW Italy). Ofioliti 46, 107–116.

Bilenker, L.D., Weis, D., Scoates, J.S., Perry, E., 2018. The application of stable fe isotopes to magmatic sulfide systems: Constraints on the fe isotope composition of magmatic pyrrhotite. Econ. Geol. 113, 1181–1192.

Blanks, D.E., Holwell, D.A., Ezad, I.S., Giuliani, A., Fiorentini, M.L., Foley, S.F., 2025. The mineralogical distribution of Ni in mantle rocks controls the fertility of magmatic Ni-sulfide systems. Miner, Depos.

Blanks, D.E., Holwell, D.A., Fiorentini, M.L., Moroni, M., Giuliani, A., Tassara, S., González-Jiménez, J.M., Boyce, A.J., Ferrari, E., 2020. Fluxing of mantle carbon as a physical agent for metallogenic fertilization of the crust. Nat. Commun. 11, 4342.

Bodinier, J.-L., Godard, M., 2003. Orogenic, ophiolitic, and abyssal peridotites. Treatise on Geochemistry 2, 568.

Bodinier, J.L., Garrido, C.J., Chanefo, I., Bruguier, O., Gervilla, F., 2008. Origin of pyroxenite-peridotite veined mantle by refertilization reactions: Evidence from the Ronda peridotite (Southern Spain). J. Petrol. 49, 999–1025.

Borghini, G., Fumagalli, P., Rampone, E., 2022. Melt-rock interactions in a veined mantle: Pyroxenite-peridotite reaction experiments at 2GPa. Eur. J. Mineral. 34, 109–129.

Borghini, G., Rampone, E., Zanetti, A., Class, C., Cipriani, A., Hofmann, A.W., Goldstein, S.L., 2016. Pyroxenite Layers in the Northern Apennines' Upper Mantle (Italy)—Generation by Pyroxenite Melting and Melt Infiltration. J. Petrol. 57, 625–653.

Borghini, G., Rampone, E., Zanetti, A., Class, C., Fumagalli, P., Godard, M., 2020. Ligurian pyroxenite-peridotite sequences (Italy) and the role of melt-rock reaction in creating enriched-MORB mantle sources. Chem. Geol. 532, 119252.

Brzozowski, M.J., Good, D.J., Wu, C., Li, W., 2021. Iron isotope fractionation during sulfide liquid evolution in Cu–PGE mineralization of the Eastern Gabbro, Coldwell Complex. Canada. Chem. Geol. 576, 120282.

Canfield, D.E., Raiswell, R., Westrich, J.T., Reaves, C.M., Berner, R.A., 1986. The use of chromium reduction in the analysis of reduced inorganic sulfur in sediments and shales. Chem. Geol. 54, 149–155.

Chen, K., Tang, M., Lee, C.T.A., Wang, Z., Zou, Z., Hu, Z., Liu, Y., 2020. Sulfide-bearing cumulates in deep continental arcs: The missing copper reservoir. Earth Planet. Sci. Lett. 531, 115971.

Chen, L., Liu, Y., Li, Y., Li, Q.L., Li, X.H., 2021. New potential pyrrhotite and pentlandite reference materials for sulfur and iron isotope microanalysis. J. Anal. at. Spectrom. 36, 1431–1440.

Cherdantseva, M., Anenburg, M., Fiorentini, M., Mavrogenes, J., 2024a. Carbonated magmatic sulfide systems: Still or sparkling? Sci. Adv. 10, eadl3127.

Cherdantseva, M., Fiorentini, M.L., Fisher, C.M., Kemp, A.I.S., Martin, L.A.J., Aleshin, M., Roberts, M.P., 2025. Trace element and isotope composition of calcite, apatite, and zircon associated with magmatic sulfide globules. Miner. Depos. 60, 605–629.

Cherdantseva, M., Vishnevskiy, A., Jugo, P.J., Martin, L.A.J., Aleshin, M., Roberts, M.P., Shaparenko, E., Langendam, A., Howard, D.L., Fiorentini, M.L., 2024b. Caught in the moment: interaction of immiscible carbonate and sulfide liquids in mafic silicate magma—insights from the Rudniy intrusion (NW Mongolia). Miner. Depos. 59, 733–755.

Ciazela, J., Dick, H.J.B., Koepke, J., Pieterek, B., Muszynski, A., Botcharnikov, R., Kuhn, T., 2017. Thin crust and exposed mantle control sulfide differentiation in slow-spreading ridge magmas. Geology 45, 935–938.

Ciazela, J., Koepke, J., Dick, H.J.B., Botcharnikov, R., Muszynski, A., Lazarov, M., Schuth, S., Pieterek, B., Kuhn, T., 2018. Sulfide enrichment at an oceanic crust-mantle transition zone: Kane Megamullion (23°N, MAR). Geochim. Cosmochim. Acta 230, 155–189.

Craddock, P.R., Warren, J.M., Dauphas, N., 2013. Abyssal peridotites reveal the near-chondritic Fe isotopic composition of the Earth. Earth Planet. Sci. Lett. 365, 63–76.

Dantas, C., Ceuleneer, G., Gregoire, M., Python, M., Freydier, R., Warren, J., Dick, H.J.B., 2007. Pyroxenites from the Southwest Indian Ridge, 9-16°E: Cumulates from incremental melt fractions produced at the top of a cold melting regime. J. Petrol. 48, 647–660.

Decarlis, A., Ceriani, A., Zanetti, A., Abimbola, C.O., Tribuzio, R., 2023. The Ivrea-Verbano tectonic evolution: The role of the crust- mantle interactions in rifting localization. Earth-Science Rev. 238, 104318.

Ding, S., Dasgupta, R., 2017. The fate of sulfide during decompression melting of peridotite – implications for sulfur inventory of the MORB-source depleted upper mantle. Earth Planet. Sci. Lett. 459, 183–195.

Ding, X., Ripley, E.M., Wang, W., Li, C., Huang, F., 2019. Iron isotope fractionation during sulfide liquid segregation and crystallization at the Lengshuiqing Ni-Cu magmatic sulfide deposit. SW China. Geochim. Cosmochim. Acta 261, 327–341.

Djon, M.L.N., Barnes, S.J., 2012. Changes in sulfides and platinum-group minerals with the degree of alteration in the Roby, Twilight, and High Grade Zones of the Lac des Iles Complex, Ontario. Canada. Miner. Depos. 47, 875–896.

Downes, H., 2007. Origin and significance of spinel and garnet pyroxenites in the shallow lithospheric mantle: Ultramafic massifs in orogenic belts in Western Europe and NW Africa. Lithos 99, 1–24.

Ezad, I.S., Blanks, D.E., Foley, S.F., Holwell, D.A., Bennett, J., Fiorentini, M.L., 2024a. Lithospheric hydrous pyroxenites control localisation and Ni endowment of magmatic sulfide deposits. Miner. Depos. 59, 227–236.

Ezad, I.S., Saunders, M., Shcheka, S.S., Fiorentini, M.L., Gorojovsky, L.R., Förster, M.W., Foley, S.F., 2024b. Incipient carbonate melting drives metal and sulfur mobilization in the mantle. Sci. Adv. 10, eadk5979.

Fang, S., Huang, J., Ackerman, L., Zhang, X., Huang, F., 2024. Copper migration and enrichment in the mantle wedge: Insights from orogenic peridotites and pyroxenites. Geochim. Cosmochim. Acta 380, 83–95.

Farquhar, M.L., Charnock, J.M., England, K.E.R., Vaughan, D.J., 1996. Adsorption of Cu (II) on the (0001) plane of mica: A REFLEXAFS and XPS study. J. Colloid Interface Sci. 177, 561–567.

Fiege, A., Holtz, F., Shimizu, N., Mandeville, C.W., Behrens, H., Knipping, J.L., 2014. Sulfur isotope fractionation between fluid and andesitic melt: An experimental study. Geochim. Cosmochim. Acta 142, 501–521.

Fiorentini, M.L., LaFlamme, C., Denyszyn, S., Mole, D., Maas, R., Locmelis, M., Caruso, S., Bui, T.H., 2018. Post-collisional alkaline magmatism as gateway for metal and sulfur enrichment of the continental lower crust. Geochim. Cosmochim. Acta 223, 175–197.

Galán, G., Cruz, E., Fernández-Roig, M., Martínez, F.J., Oliveras, V., 2016. Mineral associations and major element compositions of base metal sulphides from the subcontinental lithospheric mantle of NE Spain. Mineral. Petrol. 110, 87–101.

Garuti, A., Fiandri, G., Rossi, A.P., 1986. Sulfide composition and phase relations in the Fe-Ni-Cu ore deposits of the Ivrea-Verbano basic complex (western Alps, Italy). Miner. Depos. 34, 22–34.

Garuti, G., Bea, F., Zaccarini, F., Montero, P., 2001. Age, geochemistry and petrogenesis of the ultramafic pipes in the Ivrea Zone, NW Italy. J. Petrol. 42, 433–457.

Garuti, G., Gorgoni, C., Sighinolfi, G.P., 1984. Sulfide mineralogy and chalcophile and siderophile element abundances in the Ivrea-Verbano mantle peridotites (Western Italian Alps). Earth Planet. Sci. Lett. 70, 69–87.

Handy, M.R., Franz, L., Heller, F., Janott, B., Zurbriggen, R., 1999. Multistage accretion and exhumation of the continental crust (Ivrea crustal section, Italy and Switzerland). Tectonics 18, 1154–1177.

Hattori, K.H., Arai, S., Clarke, B., 2002. Selenium, tellurium, arsenic and antimony contents of primary mantle sulfides. Can. Mineral. 40, 637–650.

Helmy, H.M., Botcharnikov, R., Ballhaus, C., Deutsch-Zemlitskaya, A., Wirth, R., Schreiber, A., Buhre, S., Häger, T., 2021. Evolution of magmatic sulfide liquids: how and when base metal sulfides crystallize? Contrib. to Mineral. Petrol. 176, 107.

Holwell, D.A., Fiorentini, M.L., Knott, T.R., McDonald, I., Blanks, D.E., Campbell, M.T., Gorczyk, W., 2022. Mobilisation of deep crustal sulfide melts as a first order control on upper lithospheric metallogeny. Nat. Commun. 13, 573.

Holwell, D.A., McDonald, I., 2010. A review of the behaviour of platinum group elements within natural magmatic sulfide ore systems. Platin. Met. Rev. 54, 26–36.

Horn, I., von Blanckenburg, F., Schoenberg, R., Steinhoefel, G., Markl, G., 2006. In situ iron isotope ratio determination using UV-femtosecond laser ablation with application to hydrothermal ore formation processes. Geochim. Cosmochim. Acta 70, 3677–3688.

Huang, J., Huang, F., Wang, Z., Zhang, X., Yu, H., 2017. Copper isotope fractionation during partial melting and melt percolation in the upper mantle: Evidence from massif peridotites in Ivrea-Verbano Zone. Italian Alps. Geochim. Cosmochim. Acta 211, 48–63.

Jenner, F.E., Arculus, R.J., Mavrogenes, J.A., Dyriw, N.J., Nebel, O., Hauri, E.H., 2012. Chalcophile element systematics in volcanic glasses from the northwestern Lau Basin. Geochemistry, Geophys. Geosystems 13, Q06014.

Jenner, F.E., O'Neill, H.S.C., 2012. Analysis of 60 elements in 616 ocean floor basaltic glasses. Geochemistry, Geophys. Geosystems 13, Q02005.

Jesus, A.P., Mateus, A., Benoit, M., Tassinari, C.C.G., Bento dos Santos, T., 2020. The timing of sulfide segregation in a Variscan synorogenic gabbroic layered intrusion (Beja, Portugal): Implications for Ni-Cu-PGE exploration in orogenic settings. Ore Geol. Rev. 126, 103767.

LaFlamme, C., Martin, L., Jeon, H., Reddy, S.M., Selvaraja, V., Caruso, S., Bui, T.H., Roberts, M.P., Voute, F., Hagemann, S., Wacey, D., Littman, S., Wing, B., Fiorentini, M., Kilburn, M.R., 2016. In situ multiple sulfur isotope analysis by SIMS of pyrite, chalcopyrite, pyrrhotite, and pentlandite to refine magmatic ore genetic models. Chem. Geol. 444, 1–15.

Lee, C.-T.-A., Luffi, P., Chin, E.J., Bouchet, R., Dasgupta, R., Morton, D.M., Le Roux, V., Yin, Q., Jin, D., 2012. Copper Systematics in Arc Magmas and Implications for Crust-Mantle Differentiation. Science 80). 336, 64–68.

Li, R., Xia, X.P., Chen, H., Wu, N., Zhao, T., Lai, C., Yang, Q., Zhang, Y., 2020. A Potential New Chalcopyrite Reference Material for Secondary Ion Mass Spectrometry Sulfur Isotope Ratio Analysis. Geostand. Geoanalytical Res. 44, 485–500.

Li, Y., Liu, J., 2006. Calculation of sulfur isotope fractionation in sulfides. Geochim. Cosmochim. Acta 70, 1789–1795.

Liu, S., Li, Y., Li, M., Yang, Z., Liu, J., Shen, Y., 2022. Equilibrium fractionation of S, Fe, and Ni isotopes in Fe-Ni sulfides: A first-principles investigation. Chem. Geol. 610, 121100.

Locmelis, M., Fiorentini, M.L., Rushmer, T., Arevalo, R., Adam, J., Denyszyn, S.W., 2016. Sulfur and metal fertilization of the lower continental crust. Lithos 244, 74–93.

Locmelis, M., Moroni, M., Denyszyn, S.W., Webb, L.E., Fiorentini, M.L., Sessa, G., Caruso, S., Mathur, R., Nanzad, B., 2021. On the formation of magmatic sulphide systems in the lower crust by long-lived mass transfer through the lithosphere: Insights from the Valmaggia pipe, Ivrea Verbano Zone. Italy. Terra Nov. 33, 137–149.

Lorand, J.P., 1989a. Abundance and distribution of CuFeNi sulfides, sulfur, copper and platinum-group elements in orogenic-type spinel lherzolite massifs of Ariège (northeastern Pyrenees, France). Earth Planet. Sci. Lett. 93, 50–64.

Lorand, J.P., 1989b. The Cu-Fe-Ni sulfide component of the amphibole-rich veins from the Lherz and Freychinède spinel peridotite massifs (Northeastern Pyrenees, France): A comparison with mantle-derived megacrysts from alkali basalts. Lithos 23, 281–298.

Lorand, J.P., Keays, R.R., Bodinier, J.L., 1993. Copper and noble metal enrichments across the lithosphere-asthenosphere boundary of mantle diapirs: Evidence from the lanzo lherzolite massif. J. Petrol. 34, 1111–1140.

Lorand, J.P., Luguet, A., 2016. Chalcophile and Siderophile Elements in Mantle Rocks: Trace Elements Controlled By Trace Minerals. Rev. Mineral. Geochemistry 81, 441–488.

Lorand, J.P., Pattou, L., Gros, M., 1999. Fractionation of Platinum-group elements and gold in the upper mantle: A detailed study in Pyrenean orogenic lherzolites. J. Petrol. 40, 957–981.

Mansur, E.T., Barnes, S.J., Duran, C.J., 2021. An overview of chalcophile element contents of pyrrhotite, pentlandite, chalcopyrite, and pyrite from magmatic Ni-Cu-PGE sulfide deposits. Miner. Depos. 56, 179–204.

Mayer, A., Mezger, K., Sinigoi, S., 2000. New Sm–Nd ages for the Ivrea–Verbano Zone, Sesia and Sessera valleys (Northern-Italy). J. Geodyn. 30 (1), 147–166.

Mazzucchelli, M., Rivalenti, G., Brunelli, D., Zanetti, A., Boari, E., 2009. Formation of highly refractory dunite by focused percolation of pyroxenite-derived melt in the Balmuccia peridotite Massif (Italy). J. Petrol. 50, 1205–1233.

McDonough, W.F., Sun, S.-s., 1995. The composition of the Earth. Chem. Geol. 120, 223–253.

Montanini, A., Tribuzio, R., 2015. Evolution of recycled crust within the mantle: Constraints from the garnet pyroxenites of the External Ligurian ophiolites (northern Apennines, Italy). Geology 43, 911–914.

Montanini, A., Tribuzio, R., Thirlwall, M., 2012. Garnet clinopyroxenite layers from the mantle sequences of the Northern Apennine ophiolites (Italy): Evidence for recycling of crustal material. Earth Planet. Sci. Lett. 351–352, 171–181.

Mukasa, S.B., Shervais, J.W., 1999. Growth of subcontinental lithosphere: evidence from repeated dike injections in the Balmuccia lherzolite massif , Italian Alps. Lithos 48, 287–316.

Obata, M., Karato, S., 1995. Ultramafic pseudotachylite from the Balmuccia peridotite, Ivrea-Verbano zone, northern Italy. Tectonophysics 242, 313–328.

Oeser, M., Strauss, H., Wolff, P.E., Koepke, J., Peters, M., Garbe-Schönberg, D., Dietrich, M., 2012. A profile of multiple sulfur isotopes through the Oman ophiolite. Chem. Geol. 312–313, 27–46.

Oeser, M., Weyer, S., Horn, I., Schuth, S., 2014. High-precision Fe and Mg isotope ratios of silicate reference glasses determined in situ by femtosecond LA-MC-ICP-MS and by solution nebulisation MC-ICP-MS. Geostand. Geoanalytical Res. 38, 311–328.

Ogunyele, A.C., Sanfilippo, A., Salters, V.J.M., Bonazzi, M., Zanetti, A., 2024. Accretion of "young" Phanerozoic subcontinental lithospheric mantle triggered by back-arc extension—the case of the Ivrea-Verbano Zone. Sci. Rep. 14, 11805.

Patkó, L., Ciazela, J., Aradi, L.E., Liptai, N., Pieterek, B., Berkesi, M., Lazarov, M., Kovács, I.J., Holtz, F., Szabó, C., 2021. Iron isotope and trace metal variations during mantle metasomatism: In situ study on sulfide minerals from peridotite xenoliths from Nógrád-Gömör Volcanic Field (Northern Pannonian Basin). Lithos 396–397, 106238.

Patten, C., Barnes, S.J., Mathez, E.A., Jenner, F.E., 2013. Partition coefficients of chalcophile elements between sulfide and silicate melts and the early crystallization history of sulfide liquid: LA-ICP-MS analysis of MORB sulfide droplets. Chem. Geol. 358, 170–188.

Pearson, D.G., 1996. Diamonds in young orogenic belts: graphitized diamond from Beni Bousera, N. Morocco, a comparison with kimberlite-derived diamond occurrences and implications for diamond genesis and exploration. African Geosci. Rev. 3, 296–316.

Pearson, D.G., Davies, G.R., Nixon, P.H., 1993. Geochemical Constraints on the Petrogenesis of Diamond Facies Pyroxenites from the Beni Bousera Peridotite Massif, North Morocco. J. Petrol. 34, 125–172.

Petermann, M., Hirschmann, M., 2003. Partial melting experiments on a MORB-like pyroxenite between 2 and 3 GPa: Constraints on the presence of pyroxenite in basalt source regions from solidus location and melting rate. J. Geophys. Res. 108, 2125.

Pieterek, B., Ciazela, J., Boulanger, M., Lazarov, M., Wegorzewski, A.V., Pańczyk, M., Strauss, H., Dick, H.J.B., Muszyński, A., Koepke, J., Kuhn, T., Czupyt, Z., France, L., 2022. Sulfide enrichment along igneous layer boundaries in the lower oceanic crust:

IODP Hole U1473A, Atlantis Bank. Southwest Indian Ridge. Geochim. Cosmochim. Acta 320, 179–206.

Pieterek, B., Tribuzio, R., Matusiak-Małek, M., Ciążela, J., Horn, I., Weyer, S., Strauss, H., Kuhn, T., Muszyński, A., 2024. Underplated melts control sulfide segregation at the continental crust-mantle transition. Commun. Earth Environ. 5, 45.

Pistone, M., Müntener, O., Ziberna, L., Hetényi, G., Zanetti, A., Nazionale, C., 2017. Report on the ICDP workshop DIVE (Drilling the Ivrea – Verbano zonE). Sci. Dril. 5, 1–10.

Polyakov, V.B., Soultanov, D.M., 2011. New data on equilibrium iron isotope fractionation among sulfides: Constraints on mechanisms of sulfide formation in hydrothermal and igneous systems. Geochim. Cosmochim. Acta 75, 1957–1974.

Python, M., Ceuleneer, G., Arai, S., 2008. Chromian spinels in mafic-ultramafic mantle dykes: Evidence for a two-stage melt production during the evolution of the Oman ophiolite. Lithos 106, 137–154.

Quick, J.E., Mainz, D., Sinigoi, S., 1995. Emplacement of mantle peridotite in the lower continental crust, Ivrea-Verbano zone, northwest Italy. Geology 23, 739–742.

Quick, J.E., Sinigoi, S., Snoke, A.W., Kalakay, T.J., Mayer, A., Peressini, G., 2003. Geologic Map of the Southern Ivrea-Verbano Zone, Northwestern Italy. USGS Geol. Investig. Ser. 27, I–2776.

Rampone, E., Borghini, G., Basch, V., 2020. Melt migration and melt-rock reaction in the Alpine-Apennine peridotites: Insights on mantle dynamics in extending lithosphere. Geosci. Front. 11, 151–166.

Ripley, E.M., Li, C., 2003. Sulfur isotope exchange and metal enrichment in the formation of magmatic Cu-Ni-(PGE) deposits. Econ. Geol. 98, 635–641.

Ripley, E.M., Li, C., Moore, C.H., Elswick, E.R., Maynard, J.B., Paul, R.L., Sylvester, P., Seo, J.H., Shimizu, N., 2011. Analytical methods for sulfur determination in glasses, rocks, minerals and fluid inclusions. Rev. Mineral. Geochemistry 73, 9–39.

Rivalenti, G., Mazzucchelli, M., Vannucci, R., Hofmann, A.W., Ottolini, L., Bottazzi, P., Obermiller, W., 1995. The relationship between websterite and peridotite in the Balmuccia peridotite massif (NW Italy) as revealed by trace element variations in clinopyroxene. Contrib. to Mineral. Petrol. 121, 275–288.

Roduit, N., 2007. JMicroVision: un logiciel d'analyse d'images pétrographiques polyvalent. Université de Genève, Section des Sciences de la Terre.

Rudnick, R.L., Fountain, D.M., 1995. Nature and composition of the continental crust: A lower crustal perspective. Rev. Geophys. 33, 267–309.

Saunders, J.E., Pearson, N.J., O'Reilly, S.Y., Griffin, W.L., 2016. Gold in the mantle: The role of pyroxenites. Lithos 244, 205–217.

Schauble, E.A., 2004. Applying Stable Isotope Fractionation Theory to New Systems. Rev. Mineral. Geochemistry 55, 65–111.

Seal, R.R., 2006. Sulfur isotope geochemistry of sulfide minerals. Rev. Mineral. Geochemistry 61, 633–677.

Sen, I.S., Bizimis, M., Sen, G., 2010. Geochemistry of sulfides in Hawaiian garnet pyroxenite xenoliths: Implications for highly siderophile elements in the oceanic mantle. Chem. Geol. 273, 180–192.

Shanks W. C. (2013) Stable Isotope Geochemistry of Mineral Deposits. In Treatise on Geochemistry: Second Edition (eds. H. D. Holland and K. K. Turekian). Elsevier. pp. 59–85.

Shaw, C.S.J., 1997. Origin of sulfide blebs in variably metasomatized mantle xenoliths, quaternary west eifel volcanic field. Germany. Can. Mineral. 35, 1453–1463.

Shervais, J.W., 1979. Thermal emplacement model for the alpine lherzolite massif at Balmuccia. Italy. J. Petrol. 20, 795–820.

Shervais, J.W., Mukasa, S.B., 1991. The Balmuccia Orogenic Lherzolite Massif. Italy. J. Petrol., 155–174.

Sinigoi, S., Comin-Chiaramonti, P., Demarchi, G., Siena, F., 1983. Differentiation of partial melts in the mantle: Evidence from the Balmuccia peridotite. Italy. Contrib. to Mineral. Petrol. 82, 351–359.

Sinigoi S., Quick J. E., Demarchi G. and Peressini G. (2010) The Sesia magmatic system eds. M. Beltrando, A. Peccerillo, M. Mattei, S. Conticelli, and C. Doglioni. J. Virtual Explor. 36, 4.

Ueda, T., Obata, M., Ozawa, K., Shimizu, I., 2020. The Ductile-to-Brittle Transition Recorded in the Balmuccia Peridotite Body, Italy: Ambient Temperature for the Onset of Seismic Rupture in Mantle Rocks. J. Geophys. Res. Solid Earth 125, e2019JB017385.

Voshage, H., Sinigoi, S., Mazzucchelli, M., Demarchi, G., Rivalenti, G., Hofmann, A.W., 1988. Isotopic constraints on the origin of ultramafic and mafic dikes in the Balmuccia peridotite (Ivrea Zone). Contrib. to Mineral. Petrol. 100, 261–267.

Wang, Z., Becker, H., 2015a. Abundances of Ag and Cu in mantle peridotites and the implications for the behavior of chalcophile elements in the mantle. Geochim. Cosmochim. Acta 160, 209–226.

Wang, Z., Becker, H., 2015b. Fractionation of highly siderophile and chalcogen elements during magma transport in the mantle: Constraints from pyroxenites of the Balmuccia peridotite massif. Geochim. Cosmochim. Acta 159, 244–263.

Wang, Z., Becker, H., Gawronski, T., 2013. Partial re-equilibration of highly siderophile elements and the chalcogens in the mantle: A case study on the Baldissero and Balmuccia peridotite massifs (Ivrea Zone, Italian Alps). Geochim. Cosmochim. Acta 108, 21–44.

Wang, Z., Becker, H., Liu, Y., Hoffmann, E., Chen, C., Zou, Z., Li, Y., 2018a. Constant Cu/Ag in upper mantle and oceanic crust: Implications for the role of cumulates during the formation of continental crust. Earth Planet. Sci. Lett. 493, 25–35.

Wang, Z., Lazarov, M., Steinmann, L.K., Becker, H., Zou, Z., Geng, X., 2018b. The distribution of lead and thallium in mantle rocks: Insights from the Balmuccia peridotite massif (Italian Alps). Am. Mineral. 103, 1185–1199.

Wang, Z., Yao, Z., Sen, J.Z., Wang, Y., 2023. Experimental Investigation on the Transport of Sulfide Driven by Melt-Rock Reaction in Partially Molten Peridotite. J. Geophys. Res. Solid Earth 128, e2022JB026065.

Wawryk, C.M., Foden, J.D., 2015. Fe-isotope fractionation in magmatic-hydrothermal mineral deposits: a case study from the Renison Sn–W deposit. Tasmania. Geochim. Cosmochim. Acta 150, 285–298.

Weyer, S., Ionov, D.A., 2007. Partial melting and melt percolation in the mantle: The message from Fe isotopes. Earth Planet. Sci. Lett. 259, 119–133.

Weyer, S., Münker, C., Mezger, K., 2003. Nb/Ta, Zr/Hf and REE in the depleted mantle: Implications for the differentiation history of the crust - mantle system. Earth Planet. Sci. Lett. 205, 309–324.

Williams, H.M., Markowski, A., Quitté, G., Halliday, A.N., Teutsch, N., Levasseur, S., 2006. Fe isotope fractionation in iron meteorites: New insights into metal-sulphide segregation and planetary accretion. Earth Planet. Sci. Lett. 250, 486–500.

Xiong, Q., Zheng, J.P., Griffin, W.L., O'Reilly, S.Y., Pearson, N.J.S., 2014. Pyroxenite dykes in orogenic peridotite from north qaidam (NE Tibet, China) track metasomatism and segregation in the mantlewedge. J. Petrol. 55, 2347–2376.

Zhang, Z.Y., Liu, C.Z., Liang, Y., Zhang, C., Liu, T., Zhang, W.Q., Bin, J.W., 2022. Decoupled Trace Element and Isotope Compositions Recorded in Orthopyroxene and Clinopyroxene in Composite Pyroxenite Veins from the Xiugugabu Ophiolite (SW Tibet). J. Petrol. 63, 1–28.

Zhao, Y., Liu, S.-A., Xue, C., Brzozowski, M.J., Chen, J., 2024. Metasomatized mantle facilitates the genesis of magmatic nickel–copper sulfide deposits in orogenic belts: A copper isotope perspective. Geochim. Cosmochim. Acta 366, 128–140.

Zhao, Y., Xue, C., Liu, S.A., Mathur, R., Zhao, X., Yang, Y., Dai, J., Man, R., Liu, X., 2019. Redox reactions control Cu and Fe isotope fractionation in a magmatic Ni–Cu mineralization system. Geochim. Cosmochim. Acta 249, 42–58.

Zou, Z., Wang, Z., Li, M., Becker, H., Geng, X., Hu, Z., Lazarov, M., 2019. Copper Isotope Variations During Magmatic Migration in the Mantle: Insights From Mantle Pyroxenites in Balmuccia Peridotite Massif. J. Geophys. Res. Solid Earth 124, 11130–11149.